

RICE UNIVERSITY

**Observation of antiferromagnetic correlations in the  
Fermi-Hubbard model**

by

**Pedro M Duarte**

A THESIS SUBMITTED  
IN PARTIAL FULFILLMENT OF THE  
REQUIREMENTS FOR THE DEGREE

**Doctor of Philosophy**

APPROVED, THESIS COMMITTEE:

---

Randall G. Hulet, *Chair*  
Fayez Sarofim Professor of Physics and  
Astronomy

---

Thomas. C. Killian  
Professor of Physics and Astronomy

---

Somebody Else  
Professor of Physics and Astronomy

HOUSTON, TEXAS  
DECEMBER 2012

## ABSTRACT

# Observation of antiferromagnetic correlations in the Fermi-Hubbard model

by

**Pedro M Duarte**

We have used the narrow  $2S_{1/2} \rightarrow 3P_{3/2}$  transition in the ultraviolet (UV) to laser cool and magneto-optically trap (MOT)  $^6\text{Li}$  atoms. Laser cooling of lithium atoms is usually performed on the  $2S_{1/2} \rightarrow 2P_{3/2}$  (D2) transition, where temperatures of twice the Doppler limit, or  $\sim 300 \mu\text{K}$  for lithium, are achieved. The linewidth of the UV transition is seven times narrower than the D2 line, resulting in a lower Doppler limit. We show that a MOT operating on the UV transition reaches temperatures as low as  $59 \mu\text{K}$ . We load 6 million atoms from this UV MOT into a 1070 nm optical dipole trap (ODT). We show that the light shift of the UV transition in the ODT is small and blue-shifted, facilitating efficient loading. Evaporative cooling of a two spin-state mixture of  $^6\text{Li}$  in the ODT produces a quantum degenerate Fermi gas with 3 million atoms in only 11 seconds.

## ACKNOWLEDGEMENTS

This work was possible thanks to the support and guidance of my adviser Randy Hulet. James Hitchcock patiently taught me most of what I know about experimental techniques in atomic physics and for that I will always be indebted to him. I am fortunate to get to think about physics alongside Russ Hart, whose pragmatism and patience are as admirable as his keen eye for data. Ernie Yang never ceases to surprise me with his fast learning ability and I thank him for his numerous contributions to our experiment after only being around for one year. I wish to also acknowledge the contributions to the early building of the experiment by Ted Corcovilos and the help I got from RQI summer students Adrien Signoles, Florian Emaury, Adam Reed, and Kevin Jourde. I wish to also acknowledge all other current and past lab members for making this a better place to work. I would also like to thank the members of my committee for taking the time to review this work.

# Table of Contents

<b>1</b>	<b>Introduction</b>	<b>1</b>
<b>2</b>	<b>Quantum Magnetism and The Fermi-Hubbard model</b>	<b>2</b>
<b>3</b>	<b>Realizing the Fermi-Hubbard model with ultracold atoms</b>	<b>3</b>
<b>4</b>	<b>Measurement techniques</b>	<b>4</b>
<b>5</b>	<b>Experimental apparatus</b>	<b>5</b>
<b>6</b>	<b>Detection of antiferromagnetic correlations</b>	<b>6</b>
<b>7</b>	<b>Conclusion</b>	<b>7</b>
<b>8</b>	<b>Introduction</b>	<b>8</b>
8.1	All-optical production of degenerate quantum gases . . . . .	9
8.2	Limit of laser cooling . . . . .	11
8.3	Outline of the thesis . . . . .	12
<b>9</b>	<b>Description of the apparatus</b>	<b>13</b>
9.1	Vacuum . . . . .	13
9.2	671 nm Magneto-optical trap . . . . .	15
9.2.1	Laser system . . . . .	15

Chapter	Page
9.2.2 Zeeman slower . . . . .	19
9.3 323 nm Magneto-optical trap . . . . .	20
9.3.1 Laser frequency stabilization . . . . .	21
9.3.2 Vapor cell for saturated absorption spectroscopy . . . . .	24
9.3.3 Beam waist and power balance . . . . .	29
9.4 Optical dipole trap . . . . .	30
9.5 Magnetic field . . . . .	32
9.5.1 Field control . . . . .	33
9.6 Diagnostics . . . . .	35
9.6.1 Fluorescence imaging . . . . .	35
9.6.2 Absorption imaging . . . . .	37
9.7 Control, automation, and data analysis . . . . .	40
<b>10 Narrow linewidth <math>^6\text{Li}</math> magneto-optical trap</b>	<b>43</b>
10.1 671 nm MOT . . . . .	43
10.2 323 nm MOT . . . . .	45
<b>11 All-optical production of a degenerate Fermi gas</b>	<b>51</b>
11.1 Evaporation near a Feshbach resonance . . . . .	51
11.2 Light shift measurement for our optical trap . . . . .	52
<b>12 Conclusion</b>	<b>56</b>
<b>BIBLIOGRAPHY</b>	<b>58</b>

## Introduction

---

## Quantum Magnetism and The Fermi-Hubbard model

---

# Realizing the Fermi-Hubbard model with ultracold atoms

---



## Measurement techniques

---

## Experimental apparatus

---

## Detection of antiferromagnetic correlations

---

## Conclusion

---

## Introduction

---

A degenerate Fermi gas (DFG) of atoms was first produced in 1999 [1], four years after the first Bose-Einstein condensates were produced [2–4]. The reason for the delay being principally that it is not possible to evaporatively cool identical fermions in a magnetic trap.

Evaporative cooling relies on rethermalization of the gas via elastic collisions. For a long-range interaction potential<sup>1</sup> for a partial wave  $\ell$ ,  $U(r, \ell) = -\frac{C_6}{r^6} + \frac{\ell(\ell+1)}{Mr^2}$  and the location and height of the centrifugal barrier are determined by

$$\frac{\partial U(r, \ell)}{\partial r} = 0 \quad \Rightarrow \quad U_{\text{cb}}(\ell) = \frac{1}{3(6C_6)^{1/2}} \left( \frac{\ell(\ell+1)}{M} \right)^{3/2}.$$

For  ${}^6\text{Li}$ ,  $C_6 = 1394$  a.u. [5], and  $U_{\text{cb}}(\ell)/k_{\text{B}} \approx (\ell(\ell+1))^{3/2}$  mK. At a temperature much less than  $U_{\text{cb}}(\ell)/k_{\text{B}}$ , atoms colliding with angular momentum  $\ell$  do not have enough energy to overcome the centrifugal barrier and their scattering phase shift, and hence their scattering cross section, go to zero. Therefore, at low enough temperatures only  $\ell = 0$  collisions can occur; however, for identical fermions  $\ell$  must be odd due to the required anti-symmetry of the total wavefunction. So when the temperature of a gas of identical fermions is sufficiently far below  $U_{\text{cb}}(\ell = 1)/k_{\text{B}} = 2.8$  mK the gas becomes collisionless:  $p$ -wave collisions are thermally suppressed and  $s$ -wave collisions are symmetry forbidden.

---

<sup>1</sup>Atomic units are used. In atomic units, the electron mass ( $m_e$ ), electron charge ( $e$ ), reduced Planck's constant ( $\hbar$ ), and Coulomb's constant ( $1/4\pi\epsilon_0$ ) are unity by definition. The atomic unit of length is the Bohr radius,  $a_0$ , and the atomic unit of energy is the Hartree  $e^2/4\pi\epsilon_0 a_0$ . The mass of  ${}^6\text{Li}$  in atomic units is  $m = 1.09 \times 10^4$  a.u.

This is not a problem when one confines fermions in different internal states in a magnetic trap: the Pauli exclusion principle does not rule out  $\ell = 0$  collisions for distinguishable fermions. However, when trapping fermions in two different spin states, two-body inelastic collisions, can result in loss of atoms or heating of the sample. For fermionic  $^{40}\text{K}$  atoms there is a pair of hyperfine states that are magnetically trappable and stable against spin changing collisions. It was with a mixture of these states that the first DFG of atoms was produced [1].

For  $^6\text{Li}$ , the only other radioactively stable fermionic isotope among the alkali, there are no pairs of internal states that are both magnetically trappable and stable against spin changing collisions. The suppression of  $s$ -wave collisions forces the introduction of a second atomic species in order to provide a colliding partner that will allow evaporative cooling to degeneracy. DFGs of  $^6\text{Li}$  have been obtained in this way using bosonic  $^7\text{Li}$  [6, 7],  $^{23}\text{Na}$  [8], or  $^{87}\text{Rb}$  [9] as a coolant.

## 8.1 All-optical production of degenerate quantum gases

All optical production [10–14] refers to experiments in which evaporative cooling is done in a far off-resonance optical dipole trap, without magnetic trapping. Far-detuned optical potentials can trap all ground states for a given atom, allowing selection of ground states with favorable elastic and inelastic properties as candidates to reach degeneracy. In the case of Fermi gases, this offers the ability to trap the two energetically lowest hyperfine sublevels (high-field seekers), which are stable against spin changing collisions but are not trappable in a magnetic trap. This eliminates the need for sympathetic cooling with another species and greatly simplifies the experimental setup.

Evaporative cooling in an optical trap is different than in a magnetic trap. In a

magnetic trap the tail of the Maxwell-Boltzmann distribution can be removed without changing the shape of the trapping potential by using RF radiation to drive transitions to untrapped states. This leads to runaway evaporation, where the density and the collision rate increase as the atoms get colder. In an optical dipole trap the intensity is reduced to force evaporation. Reducing the trap depth also lowers the confinement strength. This may lower the density sufficiently to lower the collision rate, thus making evaporation less efficient as it progresses<sup>2</sup>. This problem may be mitigated by using a Feshbach resonance to increase the elastic collision cross section. In the case of bosons this must be done with care, as three-body inelastic collisions can lead to rapid losses near a Feshbach resonance. For fermions in a two-state mixture, three-body inelastic collisions are suppressed due to the Pauli exclusion principle, but can become significant at high enough densities [17]. The elastic collision cross section can reach the unitarity limit<sup>3</sup> near the Feshbach resonance, leading to fast and efficient evaporation to degeneracy.

Optical traps thus provide a fast and very efficient way to evaporate spin mixtures of fermions to quantum degeneracy; however, they are not without their challenges. An essential prerequisite is a sufficiently deep optical potential; the depth is determined by the temperature of atoms being loaded into the trap. Generally, the starting point for the production of quantum gases is a magneto-optical trap (MOT). For lithium and potassium typical temperatures achievable in a MOT are roughly twice the Doppler limit, or  $300\,\mu\text{K}$ . Therefore, very large power or tightly focused optical traps are required to efficiently transfer atoms from the MOT prior to evaporation.

Quantum degenerate gases of  $^6\text{Li}$  have been realized using deep optical traps

---

<sup>2</sup> Schemes to achieve runaway evaporation in an optical trap have been demonstrated [15, 16], but they are not as simple as just lowering the trap laser power.

<sup>3</sup>Near a Feshbach resonance the  $s$ -wave scattering length diverges. The scattering cross section,  $\sigma = 4\pi a_s^2$ , cannot go to infinity because this would violate conservation of the probability current (unitarity), instead it takes the maximum allowed value which is  $4\pi/k^2$  for  $s$ -waves.

loaded from a MOT. To achieve the required trap depth, groups have used high power lasers [12] or resonator enhanced optical dipole traps [14]. The approach that I present in this thesis involves a moderate power 50 W fiber laser focused to a waist of  $73\text{ }\mu\text{m}$  and relies on narrow linewidth laser cooling of  $^6\text{Li}$  which can produce samples below  $60\text{ }\mu\text{K}$  in a MOT.

## 8.2 Limit of laser cooling

The limit to the temperature of a laser cooled sample, in a two-level atom picture, is the Doppler limit,  $T_D = \hbar\Gamma/(2k_B)$ , where  $\Gamma/(2\pi)$  is the natural linewidth of the excited state of the laser cooling transition [18, 19]. In many cases, sub-Doppler cooling can be achieved due to the multi-level character of real atoms and the limit to cooling is then the recoil temperature,  $T_R = \hbar^2k^2/(2mk_B)$ , where  $k$  is the wave number of the laser cooling light and  $m$  is the mass of the atom. Polarization gradient cooling, the most widely used sub-Doppler cooling method, is effective if the linewidth of the cooling transition is small compared to the hyperfine splitting of the excited state [20–23].

For atoms like sodium, rubidium, or cesium polarization gradient cooling [20–23], provides samples with temperatures on the order of  $10\text{ }\mu\text{K}$ . For lithium and potassium, the excited state hyperfine splitting is not well resolved and typical laser cooling temperatures are  $300\text{ }\mu\text{K}$ . At this temperature a deep optical trap is required that can capture the atoms before forced evaporation to quantum degeneracy.

In our experiment we have realized a  $^6\text{Li}$  MOT operating on the narrow yet still dipole allowed  $2S_{1/2} \rightarrow 3P_{3/2}$  transition (UVMOT). This transition has a Doppler limit of  $20\text{ }\mu\text{K}$  and a recoil limit of  $15\text{ }\mu\text{K}$  (see Fig. 9.8). We have achieved temperatures in the UVMOT as low as  $57\text{ }\mu\text{K}$ . This extra stage of laser cooling reduces the intensity



---

requirements of an optical dipole trap for lithium and also provides a higher phase space density at the start of evaporative cooling.

### 8.3 Outline of the thesis

In this thesis I start by describing the apparatus, which we refer to in the lab as Apparatus3, and the various tools that have been implemented to make possible the creation of a DFG. Chapter 10 details the procedure used to load the atoms into the UVMOT and shows results of measurements of the properties of the UVMOT. The all optical production of a degenerate gas starting from atoms in the UVMOT is presented in Chapter 11. Finally in Chapter 12 the significance of our achievements is summarized and the prospects for the future of Apparatus3 are laid out.

## Description of the apparatus

---

The experiments described in this thesis take place inside a vacuum where the pressure of the background gas is less than  $5 \times 10^{-10}$  Torr. Figure 9.1 shows the main components of the apparatus. Atoms from a thermal beam originating in the oven are decelerated by the Zeeman slower and cooled transversally by the two-dimensional magneto-optical trap (2DMOT) before being captured in the magneto-optical trap (MOT) at the center of the chamber, where the temperature can be as low as  $300 \mu\text{K}$ . We transfer the atoms to the narrow linewidth magneto-optical trap operating on the ultraviolet  $2S_{1/2} \rightarrow 3P_{3/2}$  transition (UVMOT) where they can be cooled to  $57 \mu\text{K}$ . From the UVMOT we load an optical dipole trap where the atoms are evaporated to quantum degeneracy. Evaporation is performed in the presence of a bias magnetic field of 330 G, where the scattering length is  $\sim 280a_0$ . We perform evaporative cooling at 330 G instead of near the Feshbach resonance at 834 G because we observe density dependent loss in the unitary scattering regime that is fast enough to reduce the efficiency of evaporation. In the following sections I describe the various parts of the system.

### 9.1 Vacuum

During operation, the oven (see Fig. 9.1) is heated to  $450^\circ\text{C}$  to produce a collimated beam of lithium atoms. The Zeeman slower (see Sec. 9.2.2) is constructed with a narrow tube and provides a low conductance (0.5 L/s) that can help maintain up to

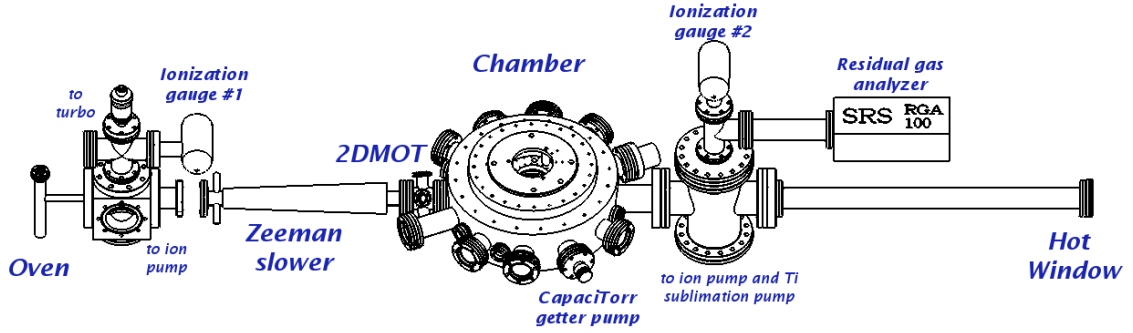


Figure 9.1: Main components of the Apparatus3 vacuum system. Gate valves between the Zeeman slower and the oven region and between the oven and the turbo pump are not shown. Ion pumps, titanium sublimation pump, and turbo pump are also not shown.

a factor of 10 pressure differential between the oven and the main chamber sections. The pressure<sup>1</sup> in the oven section is  $4 \times 10^{-9}$  Torr, and in the chamber section<sup>2</sup> is  $5 \times 10^{-10}$  Torr.

Lithium atoms that are not captured by the MOT eventually hit a sapphire window, dubbed the ‘hot window’, which is heated up to around 290°C to avoid coating it with the lithium metal. The long tube between the chamber and the hot window serves a differential pumping purpose; the tube inside is lined with a helical strip of non-evaporable getter material<sup>3</sup>.

The vacuum is maintained by two ion pumps and a non-evaporable getter pump. A VacIon Plus Starcell (150 L/s) from Varian vacuum technologies is connected to the cross between the chamber and the hot window sections. A titanium sublimation cartridge is attached to this pump. A smaller Vacion Plus Starcell (55 L/s) is connected to the cube in the oven section. A CapaciTorr B200 getter pump (90 L/s for H<sub>2</sub>) is attached directly to one of the chamber viewports. Due to the close proximity

<sup>1</sup>Measured with Bayard-Alpert type ionization gauge (Varian Type 571) labeled #1 in Fig. 9.1

<sup>2</sup>Measured with ion gauge #2

<sup>3</sup>SAES St 707/CTAM/30D, 30 mm wide strip.

of the getter pump to the atoms (8 cm) we expect the background pressure to be lower in the center of the chamber than the  $5 \times 10^{-10}$  Torr measured with ion gauge #2.

To initially pump down the system we have a TMU 071 turbo pump from Pfeiffer Vacuum (50 L/s). We currently keep this pump off because its vibration introduces interference fringes in our absorption images. A gate valve between the cube and the turbo pump remains closed but can be opened if pumping with the turbo pump is necessary. Pumping continuously with the turbo pump can reduce the pressure in the oven section by a factor of 2.

## 9.2 671 nm Magneto-optical trap

The magneto-optical trap (MOT) in our experiment is a six beam MOT loaded from a Zeeman slower plus a 2DMOT. The light for the MOT, 2DMOT, and the Zeeman slower is produced in a separate optical table and transferred to the apparatus table in optical fibers. On the apparatus table, the MOT light is split into six beams and the correct circular polarizations are set. In this section I describe the laser system used to produce the light for the MOT and the Zeeman slower, and also give technical information about our Zeeman slower. Details about the operation parameters and characteristics of the MOT are deferred to Chapter 10.

### 9.2.1 Laser system

Efficient laser cooling relies on continuous scattering of photons by the atom. In a magneto-optical trap, a lithium atom, see Fig. 9.2, that absorbs a photon on the  $2S_{1/2}, F=3/2 \rightarrow 2P_{3/2}$  transition, referred to as the trapping transition, can decay to the  $2S_{1/2}, F=1/2$  state. To maintain the continuous scattering of photons, a second

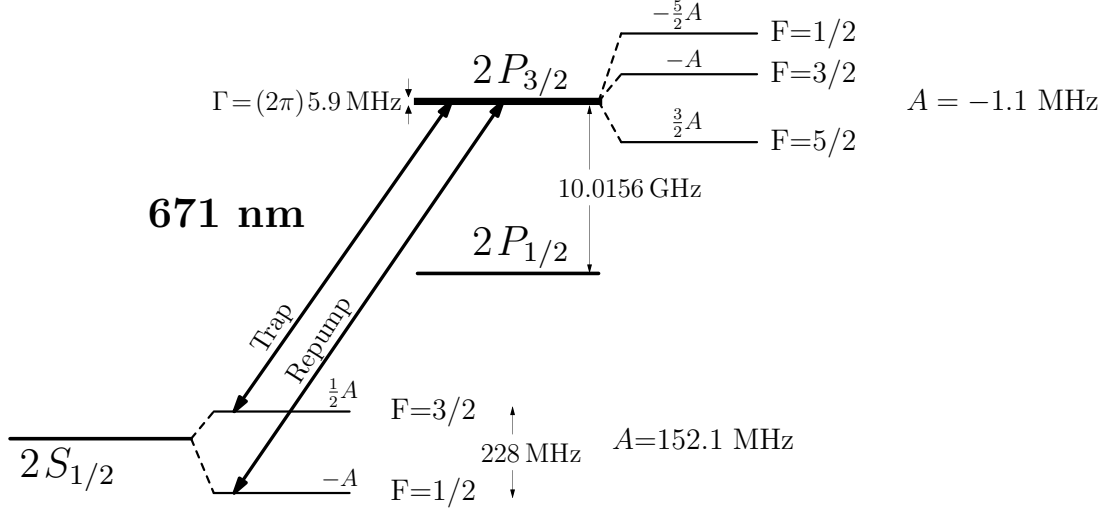


Figure 9.2: Energy level diagram showing transitions relevant for laser cooling  ${}^6\text{Li}$  using the  $2S_{1/2} \rightarrow 2P_{3/2}$  transition.

frequency that is tuned to the  $2S_{1/2}, F=1/2 \rightarrow 2P_{3/2}$  transition is required; we refer to this transition as the repumping transition. The probability of going to a dark state is higher in lithium than in other alkalis such as rubidium, cesium, or sodium because the hyperfine structure of the excited state is unresolved,  $\Gamma \approx 5|A|$ .

The laser system that is used to produce the trapping and repumping MOT light, as well as the Zeeman slower and imaging probe light, is shown in detail in Fig. 9.3. We have two extended cavity diode lasers (ECDL), which we refer to as MOT Master and ZS Master. The MOT Master is stabilized to the  $2S_{1/2}, F=3/2 \rightarrow 2P_{3/2}$  transition via saturated absorption spectroscopy (Fig. 9.4) and the ZS Master is offset locked (red detuned) to the MOT Master using the side-of-filter technique [24] (Fig. 9.5). The light from the MOT Master is split up for producing the trap and repump frequencies; each path is passed through a double-pass acousto-optic modulator (AOM) which injection-locks a slave laser diode used for amplification. The trap and repump light from the respective slaves are overlapped on a beamsplitter before injecting a tapered amplifier. The tapered amplifier output is fiber coupled to the apparatus table. After

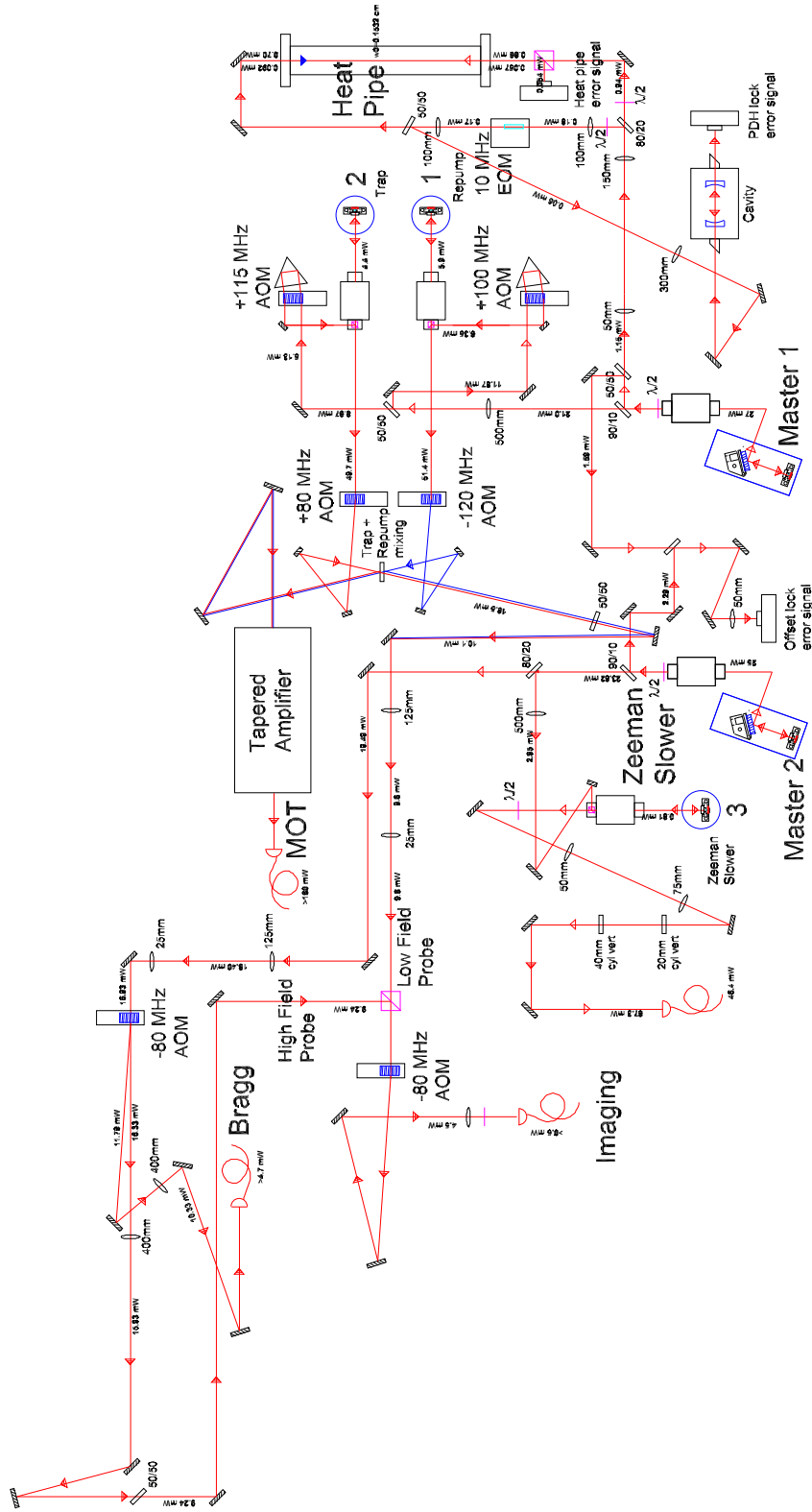


Figure 9.3: Intended for the in house reader, this figure shows the layout of the Apparatus3 671 nm laser system. Benchmark powers are indicated on the figure.

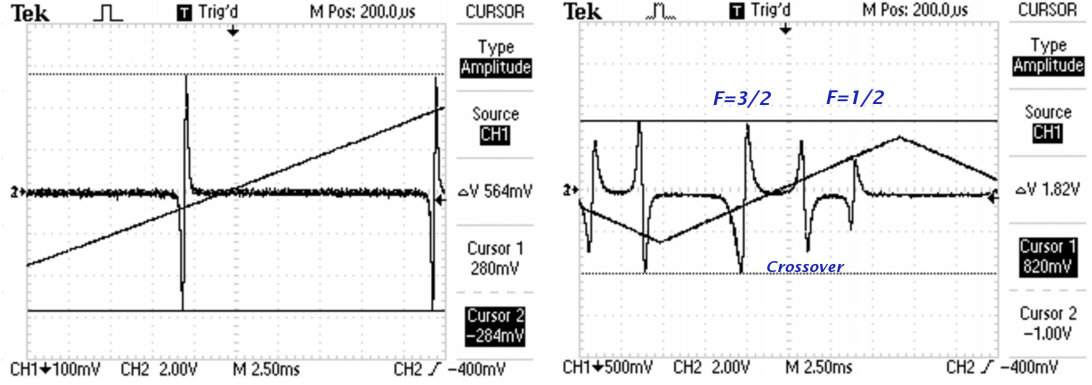


Figure 9.4: The MOT Master is stabilized to the error signal from a Fabry-Perot cavity (left). The cavity is stabilized using a saturated absorption spectroscopy error signal obtained from a lithium heat pipe. To obtain both of the error signals shown in this figure the Pound-Drever-Hall (PDH) technique is used, where the necessary sidebands are produced by phase modulation with an electro-optic modulator at 13 MHz.

passing through an AOM and splitting ten percent of the light for the 2DMOT, we can get as much as 90 mW of power. Due to the small splitting between trap and repump frequencies, 22 mW of light are produced by the tapered amplifier in unwanted sidebands at  $f_{\text{trap}} - 228 \text{ MHz}$  and  $f_{\text{repump}} + 228 \text{ MHz}$  [25]. This results in a net 53 mW of trapping light and 16 mW of repumping light that are dedicated to the MOT. Besides the loss of power we have not observed negative effects in the operation of the MOT from the presence of the sideband frequencies created by the tapered amplifier.

The ZS Master is used to produce the Zeeman slower light and the imaging probe. Light from the ECDL is split in two parts: the first path injects a slave to produce the Zeeman slower light, the second path is diverted to the imaging setup. The light from the Zeeman slower slave is coupled to an optical fiber to be transferred to the apparatus table. Light that goes to the imaging setup is passed through an AOM and coupled to a fiber to be used as the probe light for atoms at high magnetic field.

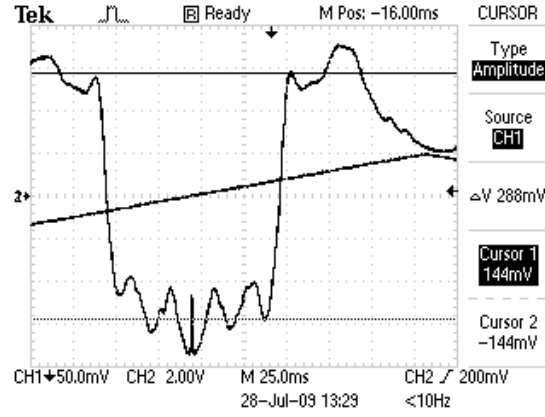


Figure 9.5: The ZS Master is stabilized using an error signal obtained using the side-of-filter technique. The zero crossing of the error signal is determined by the frequency of a local oscillator which can be tuned. In our setup we can tune ZS Master from -400 MHz to -1500 MHz with respect to MOT Master.

### 9.2.2 Zeeman slower

The Zeeman slower is effective in reducing the speed of atoms coming out of the oven to less than the capture velocity of our MOT,  $v_c \simeq 5\Gamma/k = 20$  m/s, where  $5\Gamma$  is the red detuning from resonance at which we operate the MOT during loading. The Zeeman slower works by using red detuned laser light propagating opposite to the lithium atomic beam. Due to the Doppler shift, the laser light is resonant with atoms coming out of the oven, and via repeated photon scattering can produce a maximum deceleration given by  $a_{\max} = \frac{h\Gamma}{2\lambda m}$ . As the atoms get slowed they shift out of resonance, but the magnetic field of the Zeeman slower shifts the transition to the red keeping the atoms resonant with the light as they travel through the slower.

The Zeeman slower operates on the  $\sigma^-$  transition between the  $2S_{1/2}$ ,  $m_J = -1/2$  and  $2P_{3/2}$ ,  $m_J = -3/2$  levels, shown in red in Fig. 9.6. An advantage of choosing this transition is that it is a cycling transition even at moderate magnetic fields. This eliminates the need for using repumping light in the Zeeman slower. We use a



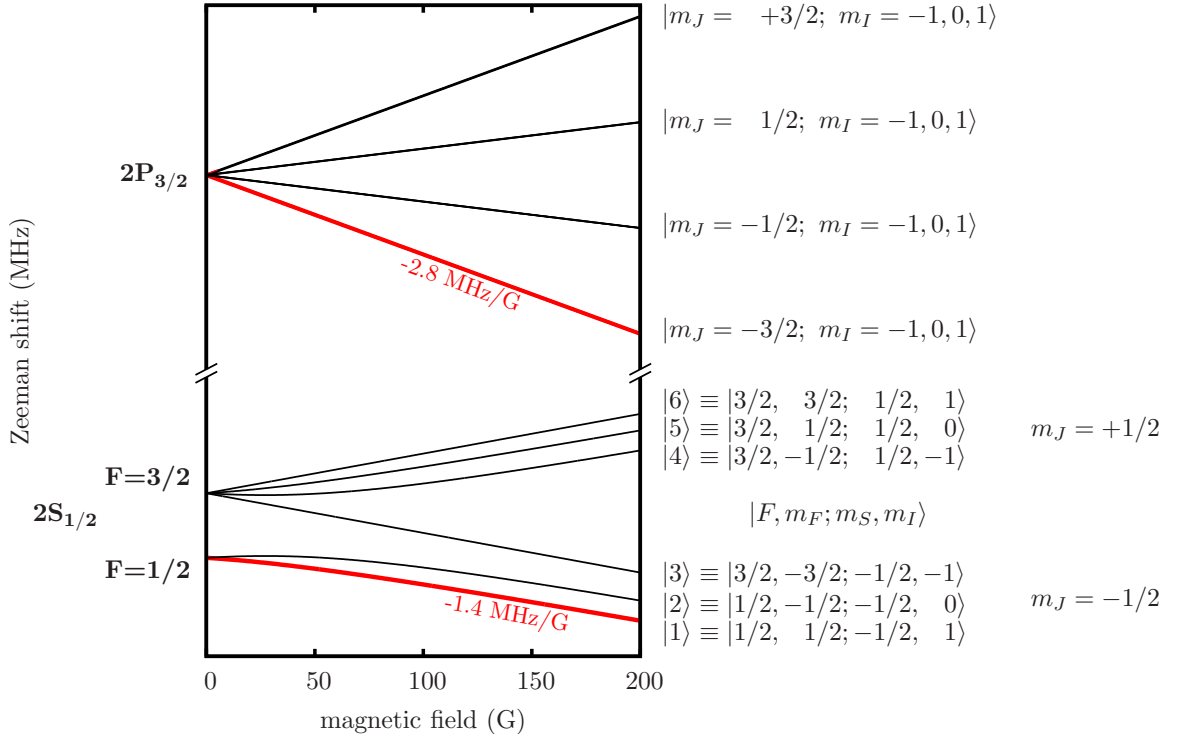


Figure 9.6: Energy level diagram of  ${}^6\text{Li}$  in a magnetic field. The red lines show the levels used in the Zeeman slower. These levels are also used for absorption imaging, see Sec. 9.6.2.

detuning<sup>4</sup> of 1540 MHz, and a magnetic field given by

$$B_z = B_0(1 - \sqrt{1 - z/L})$$

where  $B_0 \approx 800 \text{ G}$  and  $L = 34.5 \text{ cm}$ .

### 9.3 323 nm Magneto-optical trap

In this section, I explain in detail the challenges encountered while setting up the UVMOT and describe how we approached each of them; the main constraint being the limited amount of power at 323 nm, which we obtain using a commercial second harmonic generation (SHG) system from Toptica Photonics (see Fig. 9.7).

<sup>4</sup>This detuning is measured with respect to the  $F=1/2$  state. Since the lock is referenced to the  $F=3/2$  state the reading on the frequency counter of the offset lock is  $1540 - 228 = 1312 \text{ MHz}$ .

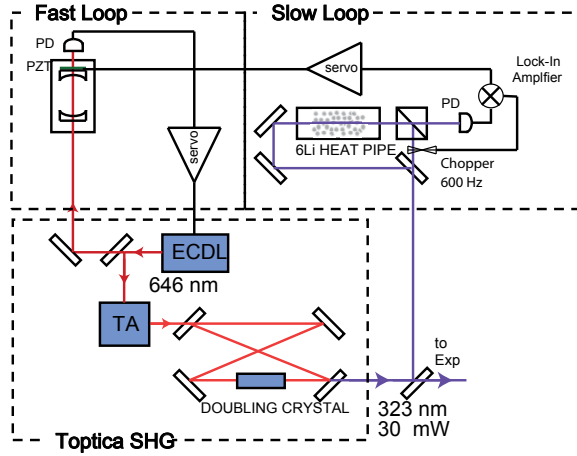


Figure 9.7: The 323 nm laser for the UVMOT is derived from a commercial TA-SHG system from Toptica Photonics. A 646 nm ECDL is amplified to 200 mW by a tapered amplifier. Light from the tapered amplifier is coupled to a doubling cavity which houses an non-linear crystal to produce the frequency doubled light at 323 nm. The doubling cavity length is stabilized using the PDH technique. The frequency modulation sidebands are created by modulating the 646 nm diode laser current. To stabilize the frequency of the 323 nm output, the 646 nm ECDL is first locked to a Fabry-Perot cavity using the PDH technique. The Fabry-Perot cavity length is stabilized so that the doubled output is resonant with the  $2S_{1/2}, F=3/2 \rightarrow 3P_{3/2}$  transition. The error signal to stabilize the cavity is obtained using saturated absorption spectroscopy.

### 9.3.1 Laser frequency stabilization

A schematic of the setup for stabilizing the 323 nm light is shown in Fig 9.7. With careful alignment, the SHG can put out 30 mW of light. The laser power slowly goes down with time, staying above 20 mW for several months. Whenever the power becomes less than 20 mW we go back and perform a careful alignment of the doubling cavity. On September 26 2011 Toptica upgraded our SHG system by installing a higher reflectivity incoupling mirror in the doubling cavity. This allowed us to increase the output power at 323 nm to 60 mW.

The stabilization of the 323 nm light to the atomic resonance involves a fast loop which locks the fundamental frequency to a Fabry-Perot cavity. This cavity is in

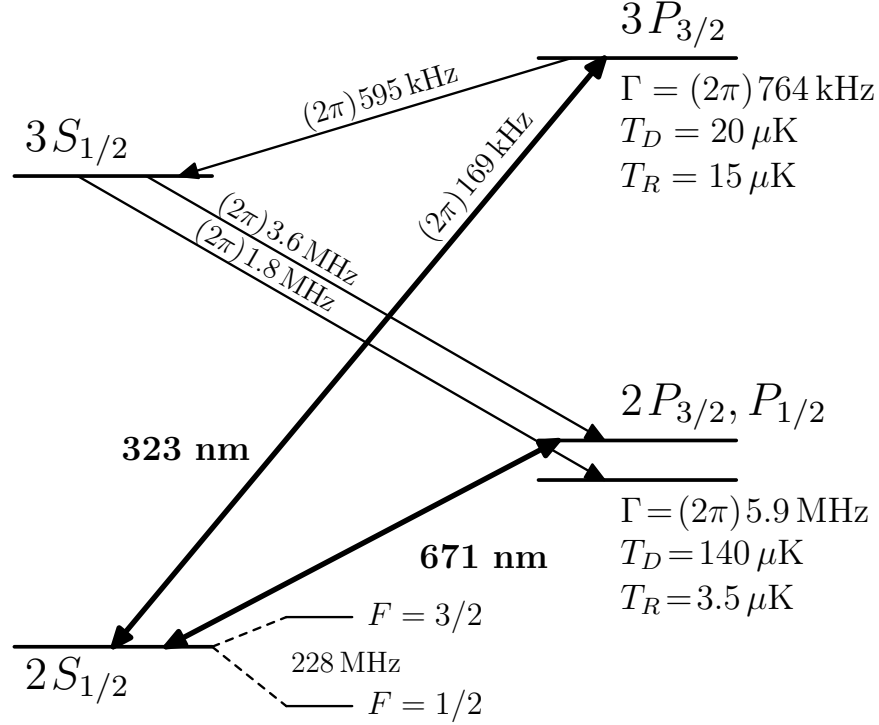


Figure 9.8: Lithium-6 energy level diagram. Lines in bold represent the transitions used to laser cool atoms. Lighter lines represent decay pathways from the excited  $3P_{3/2}$  state; the decay rates are indicated along the associated paths.

turn stabilized using a slow loop so that the output of the SHG is resonant with the  $2S_{1/2}, F=3/2 \rightarrow 3P_{3/2}$  transition (Fig. 9.8).

Saturated absorption spectroscopy is used to obtain an error signal for stabilizing the 323 nm laser. The error signal we obtain is shown in Fig. 9.9(a). When the laser is locked to the  $F=3/2$  peak, the rms linewidth is determined to be 210 kHz based on the observed noise and calibrated slope of the error signal (Fig. 9.9(b)). In order to obtain this error signal a saturated absorption setup is implemented with only about 2 mW of light. For this low power, the signal to noise ratio of the spectroscopic feature is smaller but then we can send most of the power to the experiment arm where it is used to create the UVMOT.

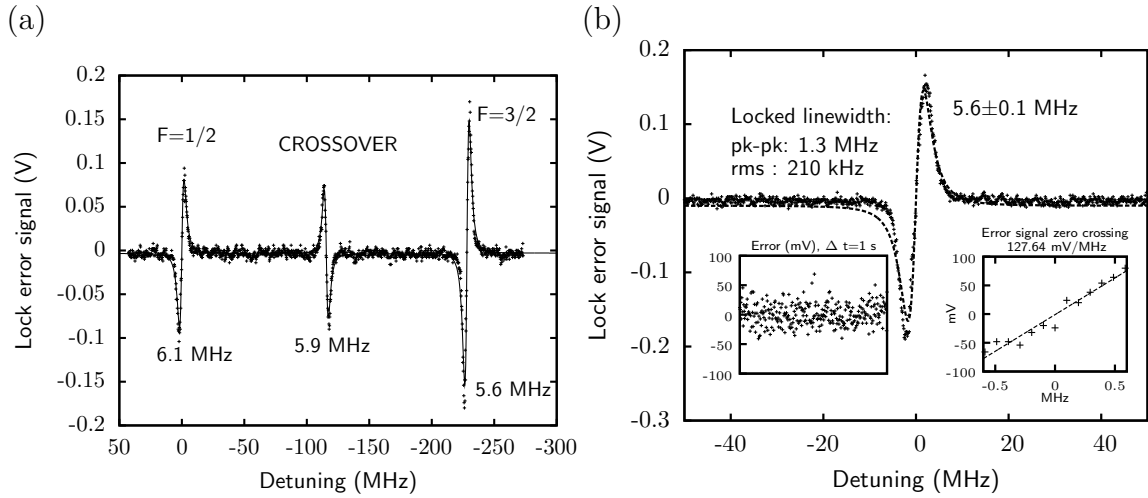


Figure 9.9: (a). Error signal used to lock the 323 nm laser to the laser cooling transition. The indicated linewidths are obtained from fits to the first derivative of a Lorentzian profile. (b). Close-up detail of the  $F=3/2$  peak. The noise on the error signal is shown when the laser is locked. From this data, taken over 1 s at a 1 kHz sampling rate, the locked linewidth is estimated given the slope of the error signal's zero crossing.

## Modulation transfer spectroscopy

To obtain the spectroscopic signal shown in Fig 9.9 we perform modulation transfer spectroscopy [26]; a schematic of the setup is shown in Fig 9.10<sup>5</sup>. The frequency of the light is modulated using a double-pass AOM. The modulation depth is  $\pm 1.5$  MHz and the modulation frequency is 35 kHz. The probe intensity, measured with the photodiode shown in Fig 9.10, is mixed with the modulation source to obtain the derivative spectrum of the Bennett hole burn in the velocity distribution by the pump beam. In this way we are able to lock the laser to the zero crossing rather than to the side of the feature.

The main disadvantage of our setup is that we apply the frequency modulation using the double pass AOM before splitting the pump and probe beams. As a con-

<sup>5</sup>More details on the electronics circuits built for this lock can be found in the undergraduate thesis of Adam Reed who helped us build the lock during his internship in the summer of 2010.

sequence, the probe beam intensity has a small residual modulation at the lock-in frequency of 35 kHz. After mixing it with the modulation source, the residual modulation shows in our error signal as an offset which can move the zero crossing up and down in an uncontrolled way. We get rid of this drifting offset by using an optical chopper, shown in Fig. 9.10 to modulate the pump beam at 600 Hz. The drifting derivative signal is mixed with the chopper reference to obtain a stable spectrum which we use to lock the 323 nm laser.

We have observed that, if only the pump is modulated, the offset of the error signal doesn't drift. Unfortunately to implement such a setup we would need a different combination of AOM's to get the correct frequencies at the atoms. For future reference, Fig. 9.11 shows a schematic of the setup if improvements were to be done.

### 9.3.2 Vapor cell for saturated absorption spectroscopy

Constructing a vapor cell for spectroscopy of lithium is more difficult than for cesium or rubidium, where an evacuated glass cell at room temperature can do the job. The vapor pressure for lithium is lower, making it necessary to heat the lithium to more than 300°C to achieve the required optical density.

In the lab we have built heat pipe ovens [27] for doing spectroscopy of lithium on the 671 nm transition. A heat pipe oven can provide a homogeneous vapor with a well defined optical density for doing spectroscopy. A heat pipe, as described in [27, 28] and shown in Fig. 9.12, works on the following basic principles:

- It has a capillary structure on its inner surface. This can be made with several layers of stainless steel mesh. The capillary structure serves as a wick: any lithium that condenses on it is returned by capillary action to the central region,

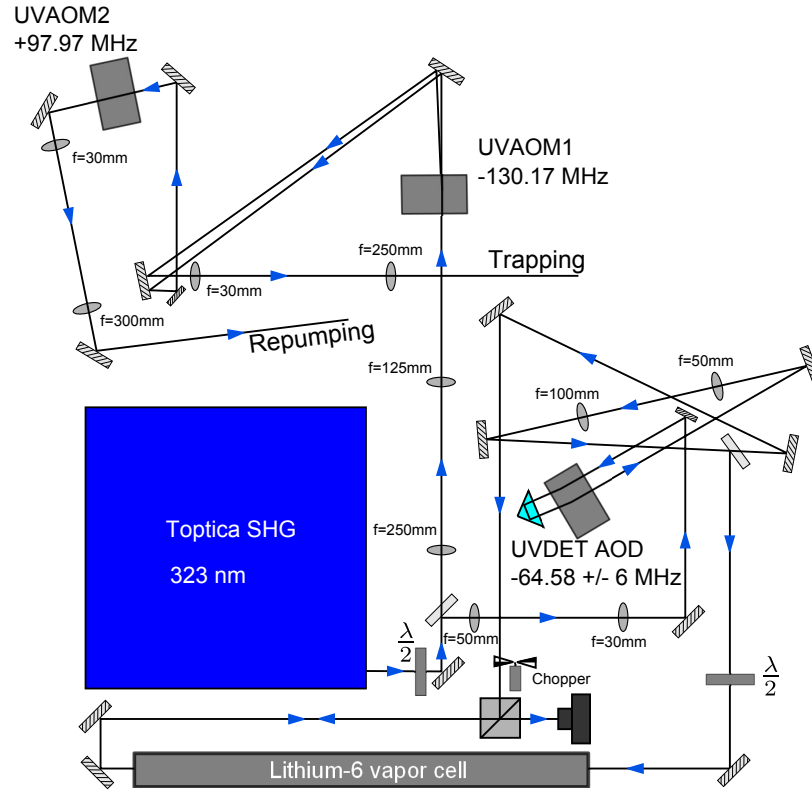


Figure 9.10: Schematic showing the optical setup for modulation transfer spectroscopy. A double-pass AOM is frequency modulated at 35 kHz. The signal from the photodiode is mixed with the modulation to obtain the modulation transfer signal. An offset due to residual amplitude modulation of the probe beam is removed by modulating the pump with a mechanical chopper at 600 Hz. The modulation transfer signal is mixed with the chopper reference frequency to obtain the error signal showed in Fig. 9.9. The AOM's are labeled with their corresponding name in the control program and the value of the frequency at which they are nominally driven. The driving frequency of the double-passed UVDET acousto-optic deflector (AOD) provides the knob for the detuning of the light used in the experiment. The trapping and repump beams are combined using 50/50 beamsplitters and used in the experiment.

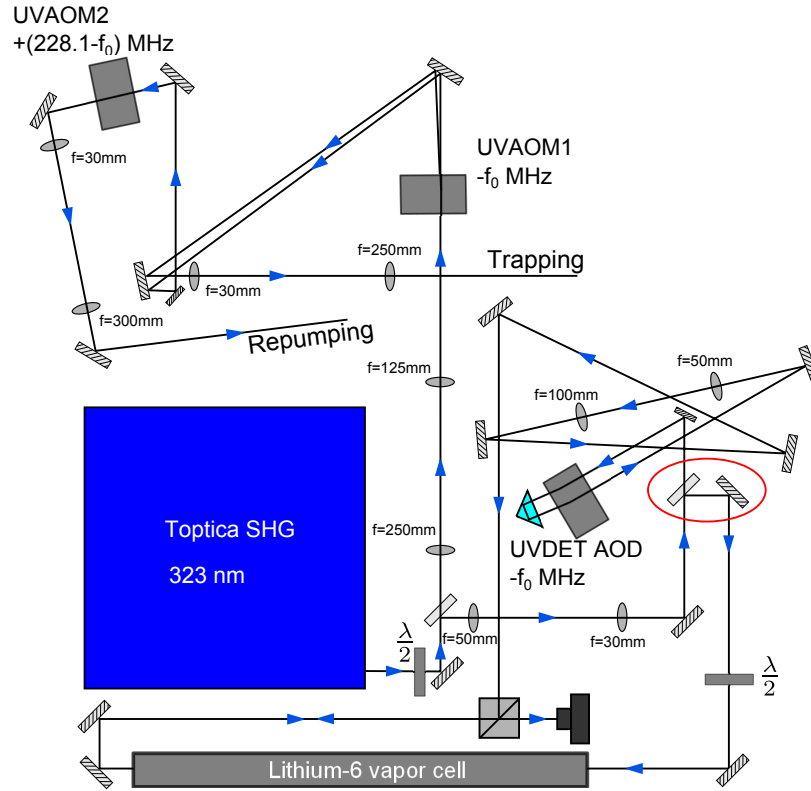


Figure 9.11: By modulating only the pump beam there is no need for a chopper to eliminate the error signal drift.  $f_0$  is the driving frequency of the double-passed UVDET AOD. The necessary frequencies for UVAOM1 and UVAOM2 are indicated as a function of  $f_0$ . The red circle emphasizes that the probe must be picked-off before passing through the UVDET AOD.

where it is heated to create a vapor.

- It is filled with an inert gas. The inert gas limits the mean free path of the metal vapor so that it cannot reach and coat the windows.

The original design of the heat pipe oven was meant for operation at high vapor pressures of up to several Torr. However, for doing saturated absorption spectroscopy with relatively narrow linewidths one needs to evacuate the heat pipe to pressures on the order of a few to a few tens of mTorr, otherwise the resulting spectrum will be affected by pressure broadening [29]; this includes the effect of velocity changing collisions which reduce the signal to noise ratio of the Doppler-free spectrum. We

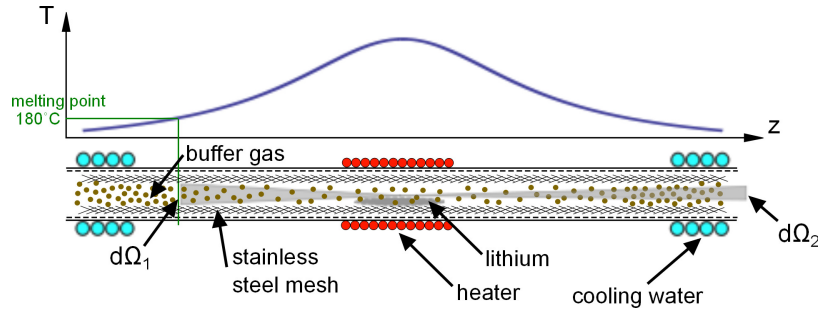


Figure 9.12: Schematic of a heat pipe oven.  $d\Omega_1$  is the solid angle for an atom to condense in a region where it will not be wicked back to the center.  $d\Omega_2$  represents the solid angle for an atom to reach the windows.

do not introduce an inert buffer gas at this pressures because the background gas<sup>6</sup> still provides a buffer to protect the windows from getting coated. One also relies on the solid angle  $d\Omega_2$  shown in Fig. 9.12, making it small to minimize the possibility of lithium reaching the windows.

The heat pipe that we used in Apparatus3 for spectroscopy on the 671 nm transition had two design issues. First, only one layer of stainless steel mesh was used. When only one layer of stainless steel mesh is used, any liquid lithium that drips through it will be in contact with the stainless steel pipe where capillary action is not effective in returning the liquid back to the heated center. Second, the temperature profile of the pipe was unsuitable for proper recirculation of the lithium via capillary action. For ideal wicking action the temperature profile of the pipe needs to be such that lithium is evaporated preferentially from the center, as shown in Fig. 9.12, and a long region of the heatpipe remains above the melting point of lithium of 180°C. This minimizes the accumulation of lithium in the regions that fall below the melting temperature.

Given our constant issues with migration of the metal to the ends in the 671 nm heat pipe, we tried a different design for the 323 nm transition. This design, shown in

<sup>6</sup>Most likely hydrogen being outgassed by the stainless steel.



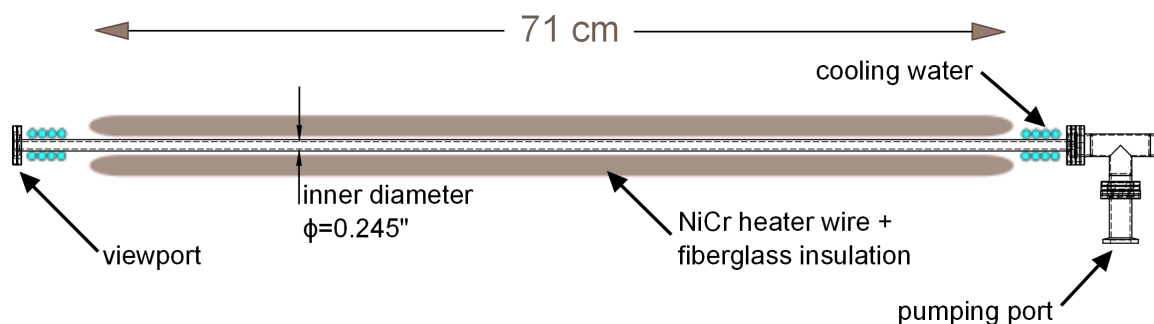


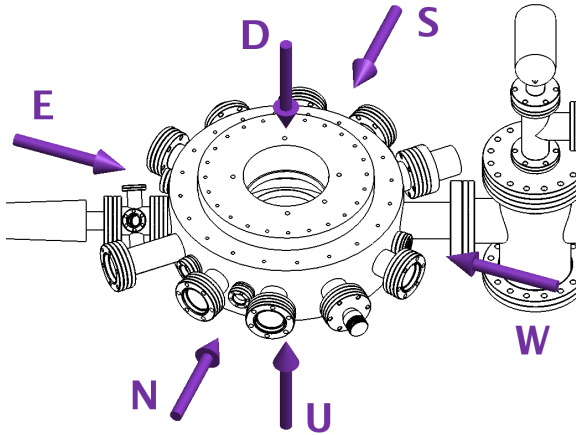
Figure 9.13: Schematic of the vapor cell used for saturated absorption spectroscopy on the 323 nm transition.

Fig. 9.13, does not have a stainless steel mesh to act as a wick, and is therefore a vapor cell rather than a heat pipe. It is made with a very narrow tube to minimize the solid angle for lithium to reach the windows. It was also made long, 71 cm, in an attempt to minimize the timescale for migration of the lithium to the cold ends. This heat pipe has been working well and at the same temperature over one year<sup>7</sup>, so we think that this design can provide a long term solution for our spectroscopic needs. Future designs may want to incorporate several layers of stainless steel mesh combined with an axially decreasing temperature profile, in order to establish wicking. A somewhat larger tube diameter will be needed to accommodate the mesh.

The spectrum obtained with the 323 nm heat pipe, which is shown in Fig. 9.9(a), is optimized at a temperature of 390°C. We observe, as it is expected [29], that the signal to noise ratio of the spectroscopic signal is better for a lower background gas pressure. When pumped with a rotary vane pump<sup>8</sup> the background gas pressure can be as low as 2 mTorr. However, after pumping is stopped, the pressure rises at a steady rate. When the pressure of the background gas goes above 25 mTorr the crossover peak is no longer visible, and above 100 mTorr the  $F=1/2$  and  $F=3/2$  peaks

<sup>7</sup>An indication of lithium migration to the cold ends is that the temperature of the center needs to be raised higher to maintain the same optical density. This means that one is raising the temperature profile to start evaporating metal that has condensed further away from the center.

<sup>8</sup>Edwards DUO 5M, pumping speed 1.7 L/s.



	% Transmission
N	68
S	87
E	75
W	58
U	40
D	40

Figure 9.14: This figure shows the percentage transmission of the 323 nm light through the viewports on our vacuum chamber. For the side viewports the losses were accounted for by measuring the power reflected back by the window. For the top and bottom viewport it was harder to make this measurement due to restricted access, so the square root of the transmission through both windows is used.

have a signal to noise ratio which makes them unsuitable for locking the laser. When this pressure is reached we pump the heat pipe back to 2 mTorr again, reducing the temperature to 200° while it is being pumped to minimize risk of coating the windows with lithium. The rate of pressure rise at the present day is about 0.5 mTorr/day, we have observed the rate gets smaller after every subsequent pumping cycle.

### 9.3.3 Beam waist and power balance

To choose the waist of the UVMOT beams we had to take into consideration the available laser power and the transmission losses on the viewports of our apparatus, shown in Fig. 9.14, which are not anti-reflection coated at 323 nm. We setup the beams so that they all have the same intensity at the atoms, thus carefully taking into account the losses at each window. This was accomplished by varying the angle of incidence on dielectric beamsplitters until the desired power ratio was achieved. Polarization beamsplitter cubes for 323 nm are expensive because they have to be optically contacted. We have observed that the UV light progressively damages the

cement used in lower priced polarizing beam-splitter cubes. We did keep one polarizing beam-splitter cube (not optically contacted) in our setup for doing the first split of the UVMOT beams. This allows some variability in the power balance without having to realign the entire system. Currently we lose 14% of the light on the mentioned cube. Considering the losses at the windows and the loss on the splitting cube we make the waist equal to 3.3 mm to achieve an intensity of  $1.0 I_{\text{sat}}$  per beam at an SHG output power of 27.4 mW.

The UVMOT uses the same viewports as the 671 nm MOT. All six beams of both wavelengths are overlapped by use of dichroic mirrors that transmit 671 nm and reflect 323 nm. We were lucky to find a long-pass filter (Part Num. NT64-634) from Edmund Optics that, at very low cost per piece, provides  $> 99\%$  reflection at 323 nm and  $> 99\%$  transmission at 671 nm for both S and P polarizations at a  $45^\circ$  angle of incidence. The UVMOT and red MOT also share an axis with the optical dipole trap. After the 671 nm and 323 nm are combined they are overlapped with the optical dipole trap light using a trichroic mirror (Custom made part from RMI Co.) that reflects IR and transmits visible. The trichroic mirrors have  $R > 99.5\%$  measured at 1064 nm and 1070 nm,  $T = 99\%$  at 671 nm and  $T = 90\%$  at 323 nm, all measured at a  $45^\circ$  angle of incidence. In the future we will implement an optical lattice which will share the top-bottom axis with the UVMOT and the red MOT; we will use the trichroic mirrors there as well.

## 9.4 Optical dipole trap

In our experiment the optical dipole trap (ODT) is used to load atoms from the UVMOT and then evaporatively cool them to degeneracy. The ODT has to be deep enough to be able to capture sufficient atoms from the MOT.

The light for the trap is provided by a broadband fiber laser operating at 1070 nm with an output power of 50 W. Two beams crossing at an angle of  $15^\circ$  and with orthogonal polarizations form a crossed beam trap, see Fig. 9.15. The second pass shares an axis with the 671 nm and 323 nm MOTs; a trichroic mirror that reflects 1070 nm is used to overlap the three wavelengths. The beams are cylindrically symmetric and focused to a  $1/e^2$  radius of  $73 \mu\text{m}$ . The trap depth is given by <sup>9</sup>

$$U_{\text{dip}}(\mathbf{r}) = \frac{\hbar\Gamma^2}{4} \left( \frac{1}{\omega_0 + \omega} + \frac{1}{\omega_0 - \omega} \right) \frac{I(\mathbf{r})}{I_{\text{sat}}}$$

The first pass through the atoms has 39 W of power and after losses at the optics and windows there are 35 W for the second pass. This gives a trap depth of  $280 \mu\text{K}$  and calculated trap frequencies of 491 Hz, 3728 Hz, and 3760 Hz. We measured the radial trap frequency by turning the dipole trap off briefly ( $40 \mu\text{s}$ ) and then turning it back on. The resulting breathing mode oscillates at twice the trap frequency and we obtain  $\omega_r = (2\pi)3.8 \text{ kHz}$ . The axial trap frequency was measured via parametric heating by sinusoidally modulating the trap depth. The number of atoms after modulation shows a loss resonant centered at twice the trap frequency. In this way we determined the axial trap frequency to be  $1/8$  of the radial trap frequency, or  $\omega_a = (2\pi)475 \text{ Hz}$ .

In order to correct for any astigmatism on the beam a CCD camera was used to take pictures of the beam profile. The lenses labeled  $E$  and  $T$  on Fig. 9.15 are mounted on gimbal mounts and can be tilted to correct for the astigmatism in the first and second waist respectively. Changing the separation between lenses  $E$  and  $F$  provides a very sensitive handle on the beam waist and it is what we used in the end to set it to the value that we desired.

---

<sup>9</sup>For lithium a single beam of power  $P$  and  $1/e^2$  beam waist  $w$  produces a trap with a depth  $U = \frac{P}{w^2} \times 38.7 \times 10^3 \mu\text{K} \mu\text{m}^2 \text{W}^{-1}$ .

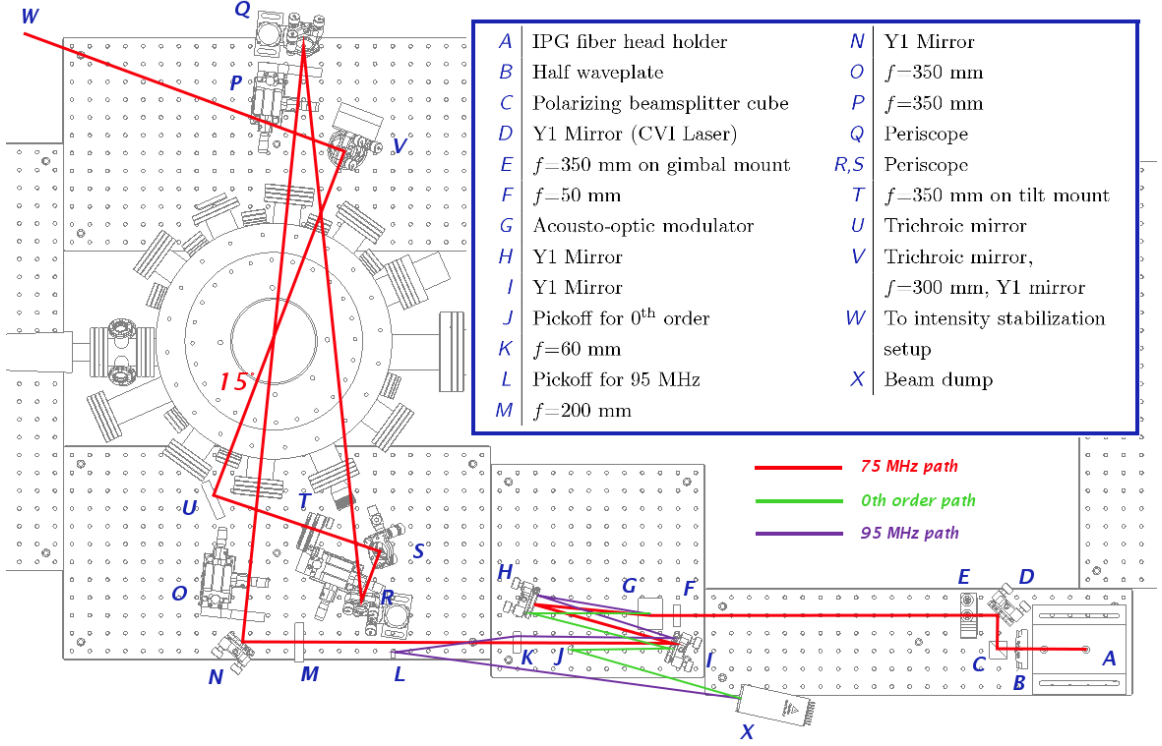


Figure 9.15: Optical dipole trap setup. The AOM can be off (green), at 75 MHz (red), and at 95 MHz (purple). For the mirrors in this setup we used Part Num. Y1-1025-45-UNP from CVI Laser, which have a damage threshold of  $10 \text{ MW/cm}^2$ . All the lens substrates are UV fused silica to reduce power dissipation and thermal lensing. The acousto-optic modulator is Part Num. 46080-2-1.06 from Neos Technologies.

In order to avoid thermal drifting of the position of our dipole trap we try to keep maximum RF power on the AOM at all times. During operation, the AOM is driven at 75 MHz. Otherwise the AOM is driven at a frequency of 95 MHz, the diffracted beam is picked off from the main path and sent to a beam dump. The undiffracted 0<sup>th</sup> order is sent to the same beam dump as shown in Fig. 9.15.

## 9.5 Magnetic field

The magnetic field in our experiment is created by a set of coils in Helmholtz configuration that are close to the atoms, inside the recessed top and bottom viewports of our vacuum chamber (Fig. 9.16). The radius of the coils is 4.72 cm, which is equal

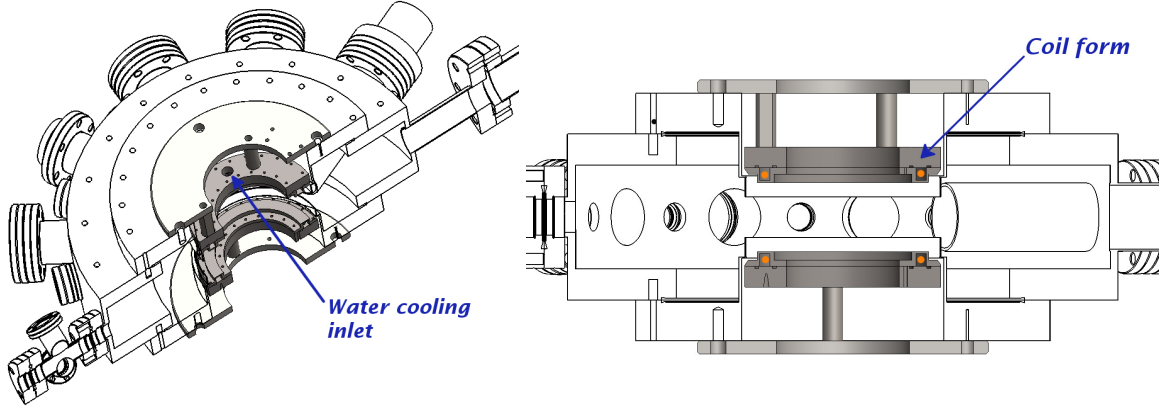


Figure 9.16: Cut-out view of our chamber showing the location of the coils that create the magnetic field. The coil forms are close to the atoms inside the re-entrant top and bottom viewports. The forms themselves are attached to a mounting plate that bolts to the re-entrant viewport flange. The coils are water cooled; only the water inlet is shown in this picture, the water outlet is on the half that is cut out.

to the separation between them. There are 35 turns on each of the coils. During the MOT stages of our experiment the current through the coils is run such that they are in anti-Helmholtz configuration and produce a magnetic field gradient along  $z$ , given by

$$dB_z = \left(\frac{4}{5}\right)^{5/2} \frac{3 \mu_0 n I}{2 r^2}$$

which is equivalent to 1.74 G/cm/A given our configuration.

After the optical dipole trap is loaded from the UVMOT the direction of the current in the top coil is reversed and they produce a bias field given by

$$B = \left(\frac{4}{5}\right)^{3/2} \frac{\mu_0 n I}{r}$$

which amounts to 6.8 G/A.

### 9.5.1 Field control

The polarity of the current on the top coil is switched by using an H-bridge made by four field-effect transistors (FETs), labeled  $Q1$  to  $Q4$  in Fig. 9.17. The current



A which can take the field up to 884 G, past the center of the Feshbach resonance at 834 G.

## 9.6 Diagnostics

In order of increasing spatial resolution and sensitivity, we can detect atoms with either a photodiode, a surveillance CCD camera, or a high performance electron multiplying CCD camera (see Fig. 9.18). We use the photodiode to monitor the fluorescence of the atoms while they are being loaded into the 671 nm MOT. It is located right in front of one of the small viewports in our chamber and a lens is used to focus the fluorescence of the atoms onto the active area. We use the surveillance camera to perform diagnostics of density and temperature in the MOT via fluorescence imaging, and the Andor EMCCD camera to take absorption images of the atoms after they have been loaded into the optical dipole trap.

### 9.6.1 Fluorescence imaging

A Navitar Zoom 7000 close-focusing macro video lens is used to focus the fluorescence from the atoms onto the CCD camera. The camera is a Basler scA100-30fm,  $1034 \times 779$  pixels with  $4.65 \times 4.65 \mu\text{m}$  pixel size. To quantitatively analyze the images taken by this camera one needs to calibrate its collection efficiency (solid angle), its magnification and its quantum efficiency.

The solid angle is measured using a big iris placed at a known distance from the atoms and then closing it up until the number of counts starts to decrease due to the iris aperture [30]. For the magnification and focusing settings that we use, the solid angle was measured to be  $g = d\Omega/4\pi = 5.55 \times 10^{-3}$ . After the magnification and focus are set, the magnification is calibrated by removing the camera from the



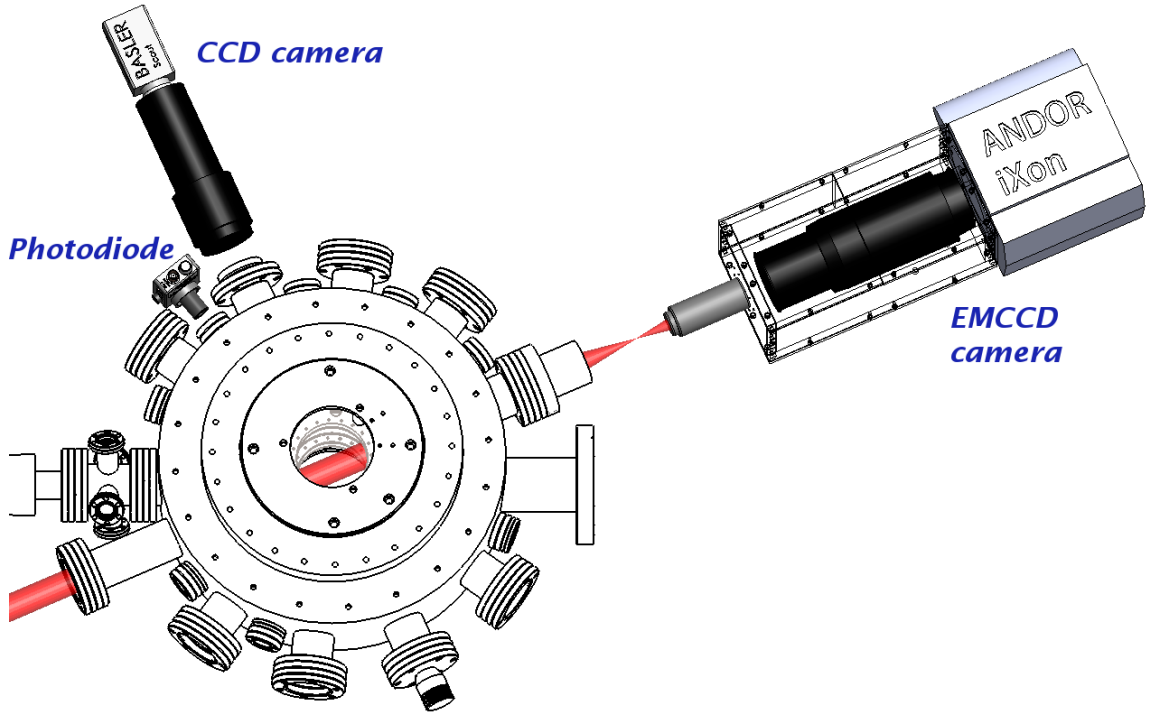


Figure 9.18: This figure shows the three instruments that we use for atom diagnostics. The photodiode is a DET36A from Thorlabs; a red filter is placed in front of the photodiode to minimize the amount of ambient light that it picks up. We obtain a signal of about 0.75 V when the MOT is fully loaded<sup>10</sup>. The surveillance CCD camera used to acquire time-of-flight images of the MOT is a Basler scA100-30fm. The scientific camera we use for absorption imaging is an Andor DU-897-E.

setup and taking a picture of a ruler placed at the distance where the atoms would be in the actual setup. The value is found to be  $m = 2.5 \times 10^{-3}$  cm/pixel. The quantum efficiency is measured by taking pictures of beam with a known power and integrating the number of counts during a certain time interval. In this way it is found that the efficiency of the camera is  $q = 13.1$  photons per count. We define the collection efficiency of the system as  $\epsilon = g/q$ .

When taking pictures of the atoms in the MOT we first release them from the trap by turning off the light and the magnetic field. After a time of flight, we pulse the MOT beams back on, typically for 100  $\mu$ s, and collect the fluorescence on the CCD. The population difference between the ground and excited state of the atoms

is assumed to be in steady state for the duration of the imaging pulse<sup>11</sup>, which means that the number of counts recorded by the CCD camera is given by

$$N_{\text{counts}} = \epsilon N_{\text{photons scattered}} = \epsilon N_{\text{atoms}} \rho_{ee} \frac{t_{\text{exp}}}{\tau}.$$

where  $\rho_{ee}$  is the fraction of atoms in the excited state and  $\tau$  is the lifetime of the excited state which for the  $2P_{3/2}$  state is  $\tau = 27.1$  ns [31]. This relationship is inverted to obtain the number of atoms in the MOT.

The factor  $\rho_{ee}$  is hard to calculate as a function of detuning in a MOT configuration with trapping and repumping frequencies. However, if the beams are on resonance,

$$\rho_{ee} = \frac{I/I_{\text{sat}}}{1 + 2I/I_{\text{sat}}}.$$

We have six beams with  $1.2 I_{\text{sat}}$  per beam, so on resonance  $\rho_{ee} \approx 0.47$ . From this value we can calibrate  $\rho_{ee}$  as a function of detuning by changing the detuning of the MOT lasers while taking pictures of atom clouds created under the same conditions.

It is useful to have a calibration of  $\rho_{ee}$  for a large detuning because the cloud of atoms can sometimes be so optically thick that the MOT beams are attenuated significantly before they reach its center. This makes the imaged distributions look artificially flat topped. Our preferred detuning for imaging dense MOT clouds is  $\Delta = -30$  MHz. We have measured the calibration factor for  $\Delta = -30$  MHz and obtained

$$\rho_{ee}(\Delta = -30 \text{ MHz}) = \frac{\rho_{ee}(\Delta = 0 \text{ MHz})}{14.9}.$$

### 9.6.2 Absorption imaging

Absorption imaging is performed by passing a collimated probe beam through the atoms; the atoms scatter light from the beam and their shadow can be imaged. In

---

<sup>11</sup>This assumption is reasonable since the exposure time is much larger than the lifetime of the excited state

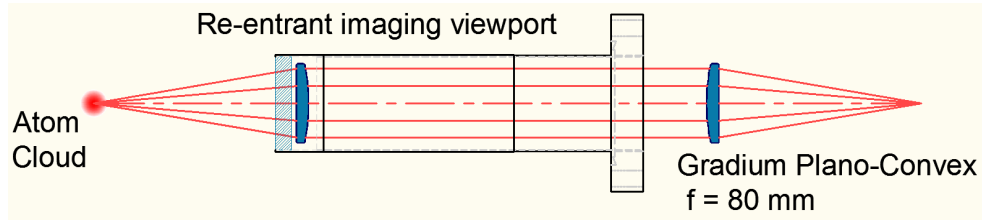


Figure 9.19: Relay lens system to form an image of the atoms outside the vacuum chamber. The lenses are gradient index plano-convex lenses, Part Num. GPX-30-80 from LightPath Technologies.

our setup the probe beam is fiber coupled to the apparatus table and then expanded to have a  $1/e^2$  beam waist of 2.75 mm. A relay lens of unity magnification (Fig. 9.19) focuses the image of the atoms onto a focal plane outside the vacuum system. The relay lens is made with two gradient index lenses; it is a simple setup which is robust to centration and variation of object distance. The numerical aperture of the relay lens system is 0.16 which gives a diffraction limited resolution of  $2.6 \mu\text{m}$  using Rayleigh's criterion. From simulations using OSLO<sup>12</sup> the relay lens with the specified gradient index profile for the individual lenses should be diffraction limited. However due to the manufacturing tolerance in the index profile we have observed this not be the case. The resolution of the relay is measured to be  $6 \mu\text{m}$  which is not as good as than the resolution obtained by the other experiments in our lab using a more complex five element custom made relay lens system.

We use an infinity corrected microscope objective and a Nikon telephoto lens to focus the relayed image on the CCD. The Nikon telephoto lens has a variable focal length of 70-300 mm. For all the data taken in this thesis we used a 5x BD Plan Apo microscope objective from Mitutoyo<sup>13</sup> and we set the Nikon telephoto at 200 mm to obtain a magnification of 5x.

<sup>12</sup>Optics Software for Layout and Optimization, Lambda Research Corporation

<sup>13</sup>Infinity corrected objectives generally specify their magnification for use with a 200 mm tube lens.

From an absorption image and a reference image the column density is obtained [32] as

$$\tilde{n}(x, z) = \frac{1}{3\pi\lambda^2} \left[ \left(1 + 4 \left(\frac{\Delta}{\Gamma}\right)^2 OD(x, z) + 2 \frac{I^{\text{ref}}(x, z)}{I_{\text{sat}}} (1 - e^{-OD(x, z)}) \right) \right]$$

where  $OD(x, z) = -\ln(I^{\text{abs}}(x, z)/I^{\text{ref}}(x, z))$ .

### High field and low field imaging

It is useful to have the ability to take absorption images of the atoms at high magnetic field as well as low magnetic field. At high magnetic field the interatomic interactions can be very large due to the wide Feshbach resonance at 834 G. On the other hand at low field the atoms are essentially non-interacting.

To image at high field, the cycling transition between the  $2S_{1/2}$ ,  $m_J = -1/2$  state to the  $2P_{3/2}$ ,  $m_J = -3/2$  is used; this is the same transition used for operation of the Zeeman slower, see Fig. 9.6. In our setup the probe beam propagates perpendicular to the quantization axis defined by the magnetic field; therefore, we can't directly drive a  $\sigma^-$  transition. The probe light has a polarization perpendicular to the magnetic field and therefore equal amounts of  $\sigma^-$  and  $\sigma^+$  light. The absorption cross section is then  $3\pi\lambda^2$  instead of the maximal  $6\pi\lambda^2$  and the saturation intensity is 10.2 mW/cm<sup>2</sup>.

When imaging at low field one faces the problem that there is no cycling transition. The probe light has to have both trapping and repump frequencies or otherwise the atoms will go into a dark state after scattering just a few photons. We overlap trapping and repump frequencies on a beamsplitter to obtain the light that seeds the tapered amplifier for the 671 nm MOT. The beams reflected off of the beamsplitter, which also come out overlapped, are passed through an AOM before being coupled to the imaging probe fiber. The low field imaging light is combined with the high field imaging light using a polarizing beamsplitter cube. Using a card to block one of the

input sides of the cube we can select between the low and high field imaging probes.

## 9.7 Control, automation, and data analysis

The experiment control system in Apparatus3 is based on the National Instruments PXI chassis NI-PXIe1062Q. The chassis hosts a 6733 Analog Output card and a 6259 Multifunction DAQ card. An experimental sequence consists of a series of TTL pulses that control the timing of events related to instruments on the apparatus. The clock to which TTL pulses are synchronized is an 80 MHz oscillator on the 6259 Multifunction DAQ card. A digital sequence can have a maximum output rate of 10 MHz (resolution time step of  $1\ \mu\text{s}$ ) and at this output rate the buffer can hold sequences that last several tens of seconds. We use the analog output channels of the PXI system as one typically uses arbitrary waveform generators; waveform outputs can be triggered by TTL pulses at any given time during the experimental sequence. The timebase for arbitrary waveform outputs on analog output channels is the on-board oscillator of each card. For the 6259 it is a 80 MHz oscillator and for the 6733 it is a 20MHz oscillator.

The experimental sequences, including all waveform outputs, are programmed in a format based on the Python programming language. This makes it very easy to program new sequences and recycle parts of old sequences. At the moment we have built up a library of 24 sequences that represent the measurements that we most commonly perform with the apparatus. Several of these sequences are benchmark measurements of the performance of every stage of the experiment that we run every day before picking up where we left the day before.

The Python based sequence code is interpreted by a program written also in Python which produces a raw sequence output file that contains all the TTL timings

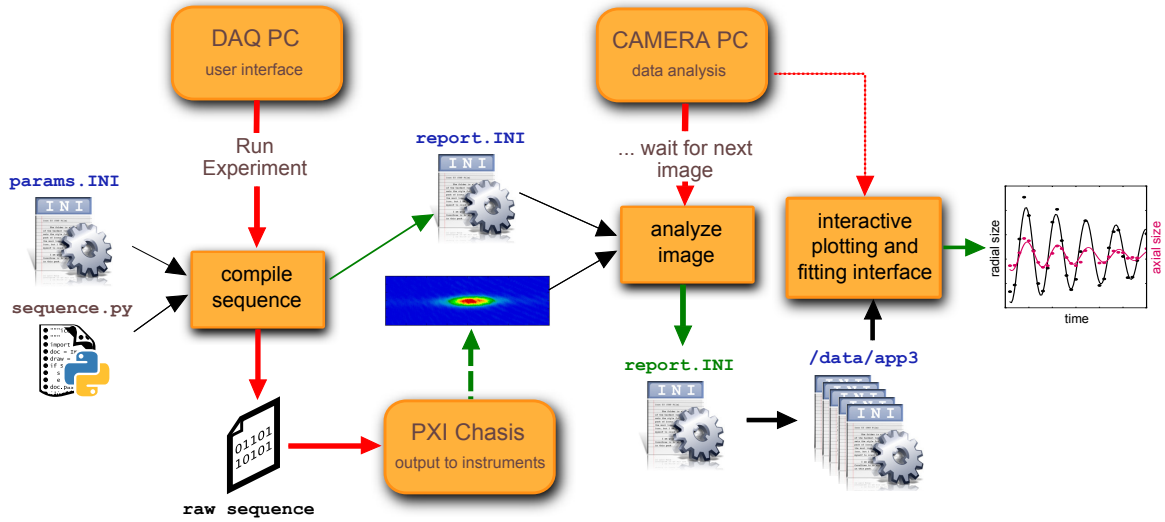


Figure 9.20: This figure attempts to show the flow of information during one experimental run. The hardware is represented by the rounded rectangles and the processes running on the hardware are represented by the straight rectangles. The red lines represent flow, the black lines represent input to a process and the green lines represent the output of a process.

When an experiment is run, the raw sequence is compiled based on the sequence file and `params.INI`. A report file is created at this time. The image of the atoms is analyzed by the camera computer and results of the analysis are stored inside `report.INI` which also contains all the parameters relevant for a given image. The plotting and fitting interface queries information from the reports on disk and produces graphs of the measured phenomena. The plot shown is the result of the measurement of the frequency of the radial breathing mode for our optical dipole trap.

and the waveforms for a particular experiment. The raw sequence output is read by LabVIEW, which takes care of outputting the sequence on the TTL and analog output channels. For most of our experiments  $t = 0$  is the moment when the MOT has loaded to a desired fluorescence, as measured by the monitoring photodiode. When the fluorescence reaches the desired level, the output of the experimental sequence is triggered.

Our scheme for taking, saving and analyzing data is based around the ubiquitous concept of the report file; it is explained in Fig. 9.20. All the parameters for all the experimental sequences in our library are stored in a file called `params.INI` that the user can edit using a regular text editor. Values are separated in sections following

the INI file convention, making it easy to scroll through the 200 long and growing parameter list. When a user runs an experiment, the sequence is compiled according to the sequence description given in the Python format file, where variables take the values indicated by `params.INI`. During compilation a copy of `params.INI` is created called `report.INI`. This report will be from then on associated with this particular shot. LabVIEW reads the compiled raw output sequence and runs the experiment; the camera computer acquires the images from the Andor camera and saves them to disk. Using information about the shot, contained in `report.INI`, the image of the atoms is analyzed and any results of the analysis, such as atom number, density, cloud size, temperature, etc., are stored in a new section inside the same report file. The report file thus contains all information relevant to a shot and the results of its analysis. An interactive plotting and fitting graphical user interface queries the report files in the data directory and allows us to see the processed data as it comes out in real time. The report file concept makes it particularly easy to revisit old data.

Analysis of the images is done in real time and as we take pictures at a rate of about 1 every 10 seconds it was necessary to write the code in C++ to avoid the analysis from hanging back. Our code is benchmarked to fit a reasonable looking cloud of atoms to a 2D-Gaussian distribution on a 512x512 pixel grid within 8-12 seconds. 1D-Gaussian fits on a row of 512 pixels take less than half a second. The graphical user interface which plots and fits data is written in Python.

## Narrow linewidth ${}^6\text{Li}$ magneto-optical trap<sup>1</sup>

---

The UVMOT cools  ${}^6\text{Li}$  atoms to a temperature of  $57\text{ }\mu\text{K}$  by cycling photons on the narrow  $2S_{1/2} \rightarrow 3P_{3/2}$  transition. In this chapter I describe the procedure to load the UVMOT and show the results of its characterization.

### 10.1 671 nm MOT

The 671 nm MOT is loaded from a Zeeman slower plus a 2DMOT. The 2DMOT is at the output of the Zeeman slower and helps collimate the slow thermal beam of atoms before it reaches the MOT. In 5 s we load  $1.4 \times 10^9$  atoms in the MOT at a temperature of  $\approx 780\text{ }\mu\text{K}$ . After loading to the desired fluorescence level we shutter the Zeeman slower laser using a hard disk drive shutter [33]. At this point we proceed to cool and compress the 671 nm MOT by reducing the intensity and detuning of the the cooling and repumping light, and increasing the magnetic field gradient to the values shown as CMOT on Table. 10.1. We take time-of-flight images of the MOT and the CMOT, and infer their temperatures by fitting the cloud sizes to a ballistic expansion as shown in Fig. 10.1.

---

<sup>1</sup>In this chapter I use  $I_{\text{sat}}^{2P} = 5.1\text{ mW/cm}^2$  for the saturation intensity of the 671 nm transition and  $I_{\text{sat}}^{3P} = 5.9\text{ mW/cm}^2$  for the saturation intensity of the 323 nm transition. Recall  $I_{\text{sat}} = \frac{2\pi\hbar c\Gamma}{3\lambda^3}$ .



	MOT	CMOT	unit
Trap intensity per beam	1.26	0.034	$I_{\text{sat}}^{2P}$
Trap detuning	-33	-12	MHz
Repump intensity per beam	0.36	0.007	$I_{\text{sat}}^{2P}$
Repump detuning	-25.2	-17	MHz
$dB_z$	22.6	26.1	G/cm
Number	1.5	1	$10^9$
$1/e$ radius	0.22	0.18	cm
Peak density	2.39	3.40	$10^{10}\text{cm}^{-3}$
Temperature	783	288	$\mu\text{K}$
Phase space density	$3.9 \times 10^{-7}$	$2.5 \times 10^{-6}$	-

Table 10.1: Comparison between the settings used for loading the 671 nm MOT and the settings after cooling and compressing (CMOT). For cooling and compressing, first the field gradient is increased in 40 ms, then after a wait of 40 ms the intensity and detuning of the beams are ramped linearly to their final values in 1 ms. The phase space density is defined as  $n_0 \lambda_T^3$  where  $n_0$  is the peak density and  $\lambda_T = \frac{h}{(2\pi m k_B T)^{1/2}}$  is the thermal de Broglie wavelength.

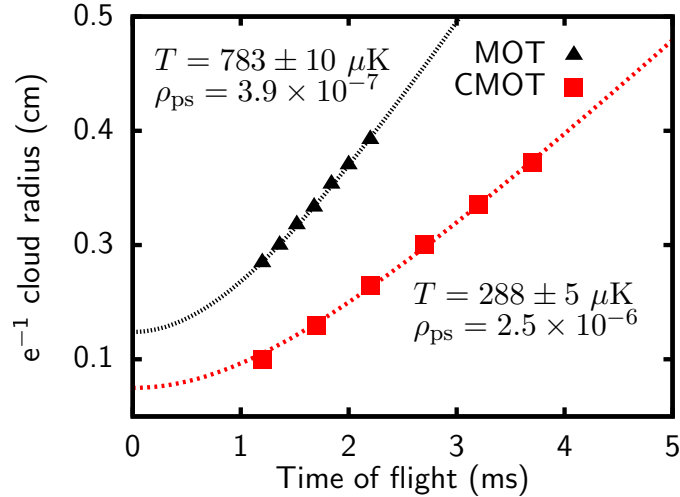


Figure 10.1: Time-of-flight expansion of atoms released from the 671 nm MOT right after loading (black triangles) and after cooling and compressing (red squares). The points represent the  $1/e$  width of Gaussian fits to the spatial profile of the freely expanding clouds. The lines are fits to ballistic expansions.

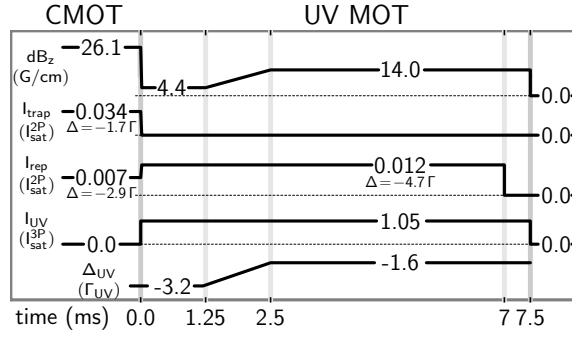


Figure 10.2: Timing diagram representing the transfer sequence from the CMOT to the UVMOT using a red repumper.

## 10.2 323 nm MOT

The first implementation of the UVMOT used repump light on the red transition instead of the UV transition. We later implemented a repump on the UV transition and found that the number of atoms loaded into the UVMOT increased by a factor of 2 and the density increased by a factor of 1.5 while the temperature stayed the same. This numbers also translated into better efficiency in loading the optical dipole trap.

### UVMOT with red repump

The UVMOT is loaded from the CMOT as shown in the timing diagram in Fig. 10.2. Loading occurs by abruptly reducing the magnetic field gradient, turning off the red cooling light, and turning on the UV cooling light. The loading phase lasts for 1.25 ms and consists of having a small magnetic field gradient to capture high velocity atoms from the red MOT. The reduction of the magnetic field gradient is critical given the narrower linewidth of the  $2S_{1/2} \rightarrow 3P_{3/2}$  transition. After the loading phase, we linearly increase the magnetic gradient and reduce the detuning of the UV cooling light over 1.25 ms. The values of this steady state UVMOT are chosen to optimize loading to an optical dipole trap as will be described in Chapter 11. After

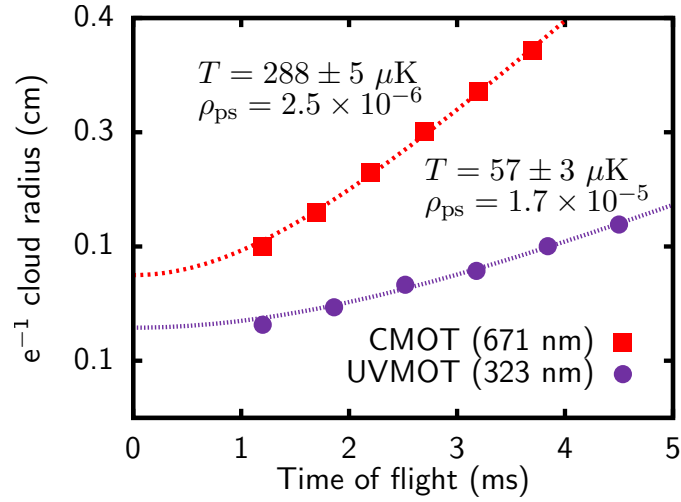


Figure 10.3: Time-of-flight expansion of the CMOT (red squares) and the UVMOT with red repump (violet circles). The points represent the  $1/e$  width of Gaussian fits to the spatial profile of the freely expanding clouds. The lines are fit to ballistic expansions.

	UVMOT	unit
Repump intensity per beam	0.012	$I_{\text{sat}}^{2P}$
Repump detuning (MHz)	-27.6	MHz
$dB_z$ Final	14	G/cm
SHG Output power	25	mW
UV intensity per beam	0.96	$I_{\text{sat}}^{3P}$
UV detuning final	-1.6	MHz
Number	2.4	$10^8$
$1/e$ radius	0.13	cm
Peak density	2.0	$10^{10} \text{ cm}^{-3}$
Temperature	57	$\mu\text{K}$
Phase space density	$1.7 \times 10^{-5}$	-

Table 10.2: Settings and results for the UVMOT with red repump.

a hold time of 5 ms the atoms are released and subsequently imaged with the Basler camera. A comparison of the performance of the CMOT and UVMOT is shown in Fig 10.3. Table 10.2 shows the settings and results for the UVMOT.

Repumping on the red transition effectively reduces the narrow line character of the UVMOT. Despite this, we still achieve  $T \ll T_D = 140 \mu\text{K}$ , most likely owing to the strength of cooling on the UV transition compared to heating on the red. The

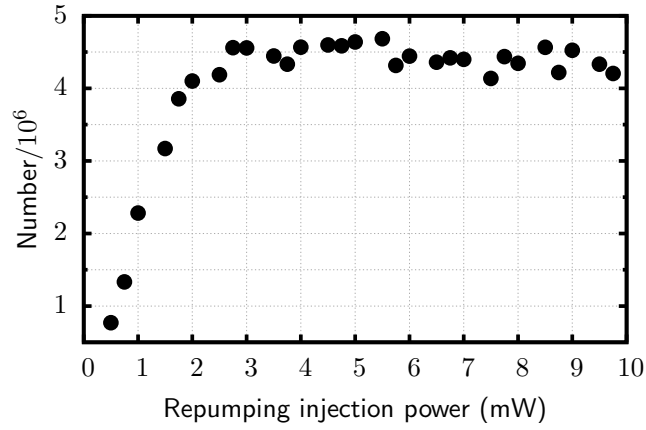


Figure 10.4: Number of atoms loaded into optical dipole trap versus injection power of red repump into the tapered amplifier. The performance of the UVMOT is not affected until the injection power goes below 3 mW. The intensity required on the red repump is only about  $I_{\text{sat}}^{2P}/100$  whereas the intensity used on the UV light is around  $I_{\text{sat}}^{3P}$ .

amount of power on the red repumping frequency that we use corresponds to only  $0.012 I_{\text{sat}}^{2P}$ , obtained with 7 mW of injection to the tapered amplifier. We observe that using less power on the red repump does not affect the performance of the UVMOT as shown in Fig. 10.4.

### UVMOT with UV repump

The timing diagram for loading the UVMOT with UV repump from the CMOT is shown in Fig. 10.5. The expansion plots and values for the parameters and results are in Fig. 10.6 and Table. 10.3 respectively.

### Effect of 323 nm power on the UVMOT

Typically  $5 \times 10^8$  atoms are captured in the UVMOT, corresponding to an efficiency of 50%. The loss of atoms is most likely due to small UV beam waists, which are smaller than the size of the atom distribution in the CMOT. The waists are limited by the total available power at 323 nm. The effect of the available power was

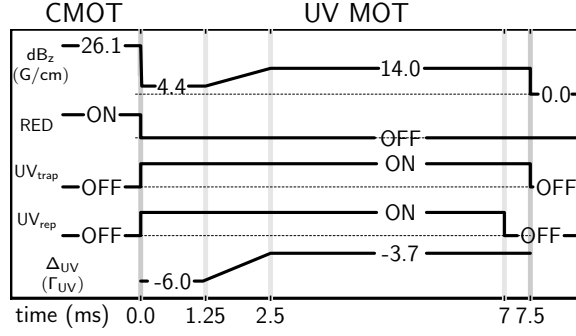


Figure 10.5: Timing diagram representing the transfer sequence from the CMOT to the UVMOT.

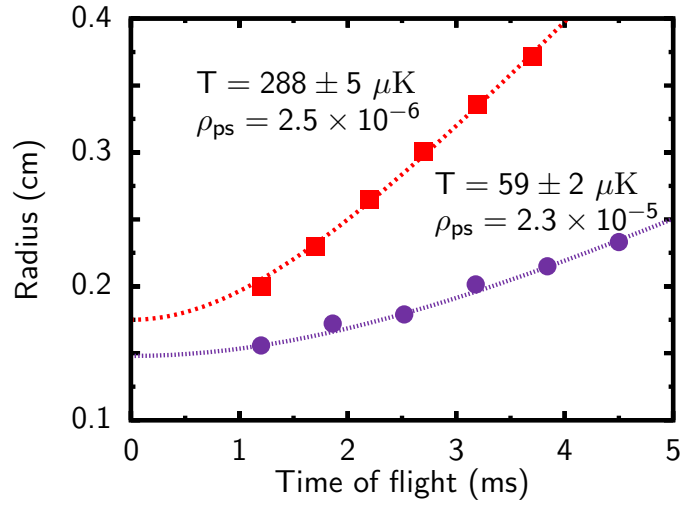


Figure 10.6: Time-of-flight expansion of the CMOT (red squares) and the UVMOT with UV repump (violet circles). The points represent the  $1/e$  width of Gaussian fits to the spatial profile of the freely expanding clouds. The lines are fit to ballistic expansions.

	UVMOT	unit
$\text{dB}_z$ Final	14	G/cm
SHG Output power	25	mW
UV trap intensity per beam	1.0	$I_{\text{sat}}^{3P}$
UV repump intensity per beam	0.1	$I_{\text{sat}}^{3P}$
UV detuning final	-1.6	MHz
Number	5.3	$10^8$
$1/e$ radius	0.15	cm
Peak density	2.9	$10^{10} \text{ cm}^{-3}$
Temperature	59	$\mu\text{K}$
Phase space density	$2.3 \times 10^{-5}$	-

Table 10.3: Settings and results for the UVMOT with UV repump.

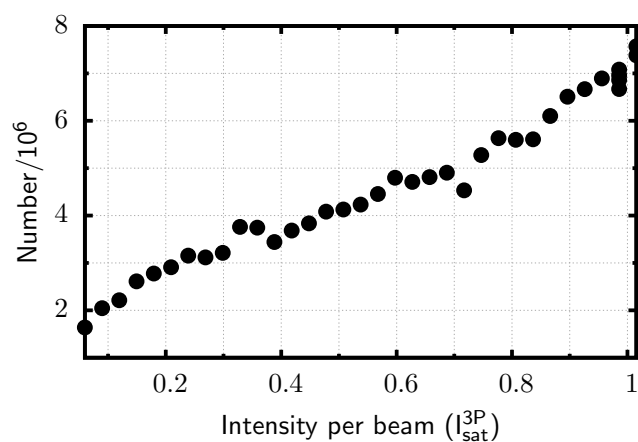


Figure 10.7: Atoms loaded into optical dipole trap (see Chapter 11) as a function of UVMOT intensity per beam. The output power of the SHG when this curve was taken was 26.7 mW, which gives a maximum of  $1.05 I_{\text{sat}}^{3P}$  per beam.

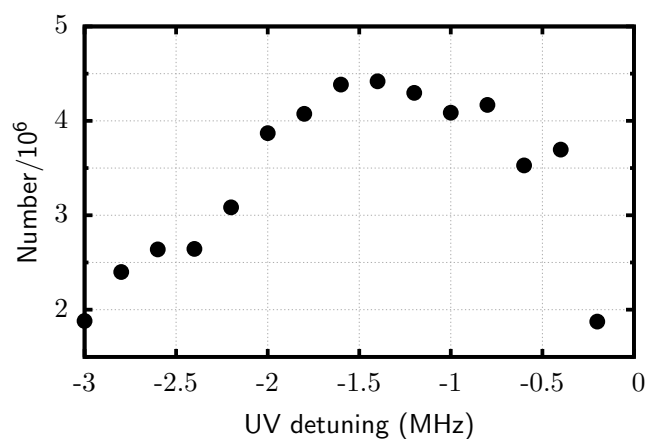


Figure 10.8: Number of atoms loaded into optical dipole trap versus UV light detuning.

studied by looking at the number of atoms loaded into the optical dipole trap as a function of UVMOT intensity. The results are shown in Fig. 10.7.

### Effect of detuning on the UVMOT

The effect of detuning of the 323 nm light on the performance of the UVMOT is shown in Fig. 10.8.

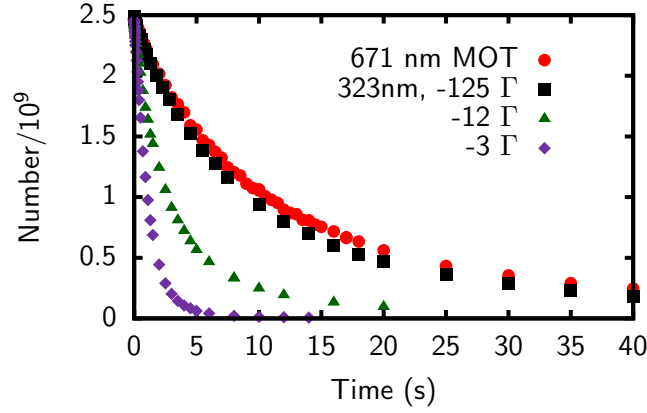


Figure 10.9: Atoms remaining in steady state red MOT as a function of time. The lifetime of the MOT is affected when UV light that is close to resonance is shined on the atoms (purple diamonds). For atoms away from the center, the UV light is blue detuned due to the magnetic field gradient of the red MOT,  $dB_z = 22.6 \text{ G/cm}$ , and causes a faster loss of atoms from the trap. Far off-resonance light has a much smaller effect on the MOT lifetime (red circles), putting an upper limit on photoionization rate. The estimated photoionization rate, for a worst case scenario cross section of  $2 \times 10^{-17} \text{ cm}^2$  [34], is less than 1 event per second.

### Photoionization

The presence of UV light presents two-photon pathways to photoionize the atom. An atom excited by the red laser to the  $2P_{3/2}$  state can be photoionized by a UV photon, or an atom excited to the  $3P_{3/2}$  state by a UV photon can be photoionized by scattering a red photon. For the case of the UVMOT with red repump we have investigated both of these processes by shining far detuned UV light on the red MOT (Fig. 10.9) or far detuned red light on the UVMOT and we do not see a reduced lifetime in either of these situations. An atom in the  $3P_{3/2}$  state could also be photoionized by scattering a UV photon. This process, however, has a significantly smaller cross section since it leaves the electron far higher in the continuum [34].

# All-optical production of a degenerate Fermi gas

---

## 11.1 Evaporation near a Feshbach resonance

After we have cooled the atoms in the UVMOT we load them into the optical dipole trap by quickly turning on the light power in the trap when we have reached the steady state values of the UVMOT, at 2.5 ms in the timing diagram shown in Fig. 10.2. We find that laser cooling on the UV transition is effective in the trap (more on this on Sec. 11.2) so we leave the UV and red repumping light on for the 5 ms following turning on the optical trap. During the last 0.5 ms of loading the red repumper is turned off to optically pump the atoms to the  $F=1/2, m_F=\pm 1/2$  states ( $|1\rangle$  and  $|2\rangle$  in Fig. 9.6). Next the UV light and magnetic field gradient are abruptly switched off.

Our experimental procedure continues by inverting the polarity of the top coil, and then energizing the coils to produce a bias magnetic field. In 20 ms we go to 330 G, where the scattering length is  $\sim -280a_0$ . We perform evaporative cooling at 330 G instead of near the Feshbach resonance at 834 G because we observe density dependent loss in the unitary scattering regime that is fast enough to reduce the efficiency of evaporation [17]. This loss is unobservable at 330 G. At  $280 a_0$  and for a sample at  $70 \mu\text{K}$   $ka \approx 1$  and the collision cross section is nearly unitarity limited which leads to efficient evaporation due to the high collision rates of the order of  $10^5$  per second [35].

We leave the trap depth at its maximum value for 200 ms and after unforced



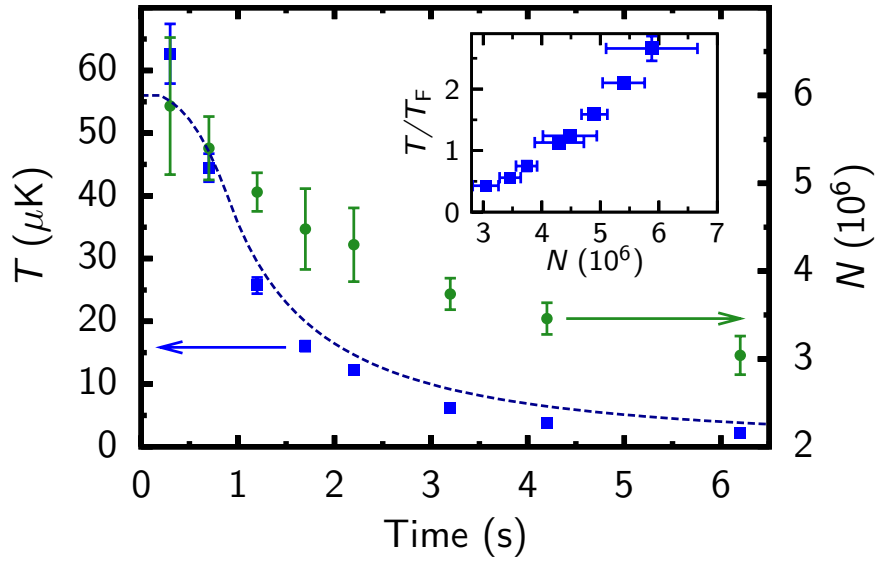


Figure 11.1: Number  $N$  (green circles) and temperature  $T$  (blue squares) of atoms in the optical trap during forced evaporation. Error bars for  $N$  are one standard deviation of the mean value of  $N$  for a sample of 5 measurements. The dotted blue line is the trap depth divided by a factor of 5, indicating the evaporation trajectory. The inset shows  $T/T_F$  for the points in the main plot. For  $T/T_F < 1$  a surface fit to a polylog [36–38] was used to determine  $T/T_F$ ; otherwise,  $T$  was measured by ballistic expansion and  $T_F$  obtained from the mean value of  $N$  and the measured trap frequencies. Systematic uncertainties in all measured quantities are estimated to be 10%.

evaporation we obtain  $6 \times 10^6$  atoms at a temperature of  $60 \mu\text{K}$ , corresponding to  $T/T_F \approx 2.7$ , where  $T_F = \hbar(\omega_r^2 \omega_a 3N)^{1/3}$ . After 6 s of forced evaporation following the evaporation trajectory shown in Fig. 11.1, a degenerate sample is obtained with  $3 \times 10^6$  atoms at  $T/T_F = 0.45$ .

## 11.2 Light shift measurement for our optical trap

Intrinsic to the capability of the UVMOT to load atoms into the dipole trap is the ability to continue to laser cool on the UV transition in the presence of the light field of the optical trap. Cooling in the optical trap only works if the AC Stark shift of the cooling transition for the wavelength of the trap light is on the order of the linewidth of the transition. It is best when the AC Stark shift vanishes altogether,

which defines the magic wavelength for the transition [39].

Our dipole trap operates at 1070 nm, close to the expected magic wavelength for the  $2S_{1/2} \rightarrow 3P_{3/2}$  transition. The polarizabilities of the  $2S$ ,  $2P$ , and  $3P$  states have been calculated by Marianna Safronova. Her results, reproduced in Fig. 11.2, show that there is a steep dependence on wavelength of the polarizability of the  $3P$  state near 1070 nm. Figure 11.3(a) shows how the differential Stark shift varies as a function of wavelength near 1070 nm for the intensity of our dipole trap. Even a small AC Stark shift of the line could be significant given the narrow linewidth of the UV transition. We find that to best load atoms to the trap we need to shift the UV cooling frequency to the blue by approximately one linewidth compared to the frequency for optimal performance of the UVMOT in free space.

We measured the differential AC Stark shift of the UV cooling transition by performing spectroscopy in the optical dipole trap. The atoms are first cooled to  $T = 3.5 \mu\text{K}$  by 6 s of forced evaporation as shown in Fig. 11.1. Following evaporation, the optical trap is adiabatically ramped to various peak intensities, and the magnetic field is then quickly ramped to zero where the atoms are illuminated by UV light with a frequency tuned near the  $2S_{1/2}$ ,  $F = 1/2$ ,  $\rightarrow 3P_{3/2}$  transition. Resonant excitation causes atoms to be optically pumped out of the  $F = 1/2$  ground state. The population remaining in  $|2\rangle$  is subsequently measured by absorption imaging. Spectra are recorded at several trap intensities, and the center of each is found by fitting to a Gaussian. These resonance locations are displayed as a function of peak intensity in Fig. 11.3(b). We find that at full trap depth, the UV transition is shifted to a 750 kHz greater frequency than for free space. This is consistent with our observation that atoms are most efficiently loaded from the UV MOT when the UV laser frequency is shifted to the blue by approximately one linewidth. With this detuning the temperature of atoms loaded into the optical trap is  $70 \mu\text{K}$ , close to the

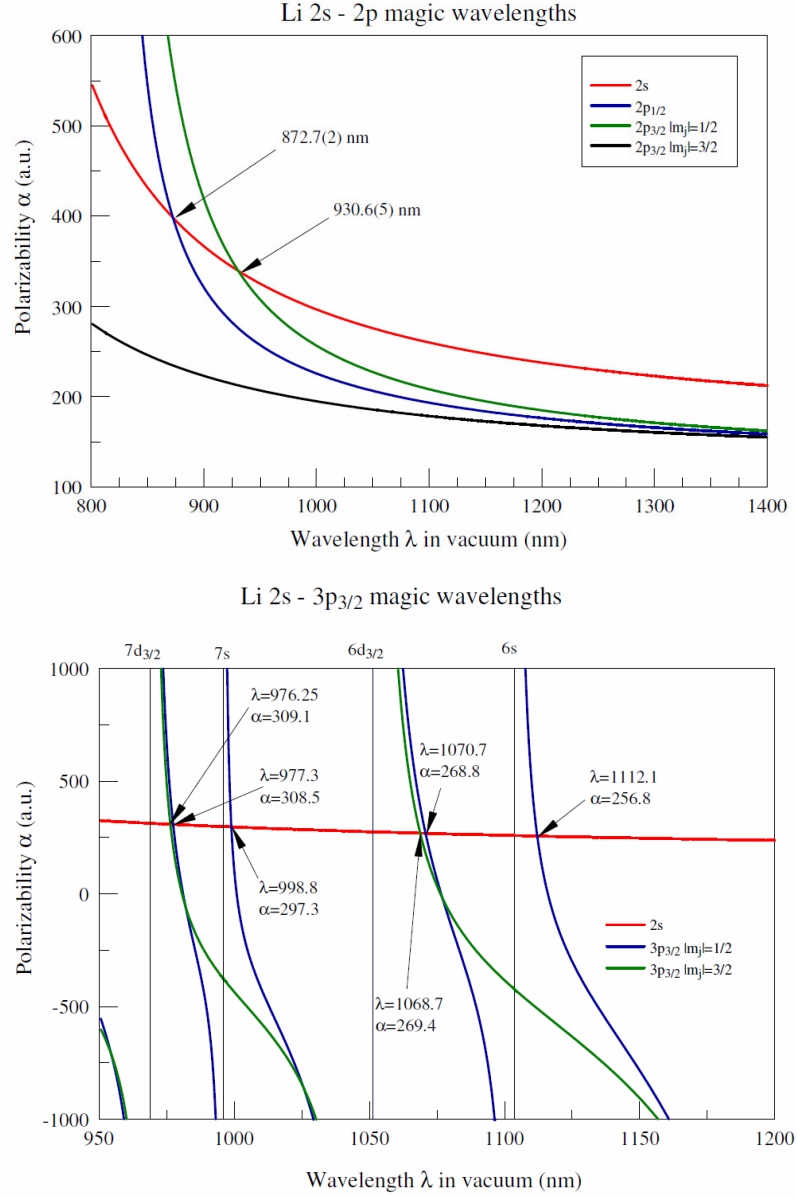


Figure 11.2: (Top) Polarizability in atomic units for the 2S and 2P states. Magic wavelengths are indicated by the arrows. (Bot) Polarizability in atomic units of the 2S and 3P states. The atomic units for polarizability can be converted to SI units ( $\text{C m}^2 \text{V}^{-1}$ ) by multiplying by  $1.648 \times 10^{-41}$  [40, 41].

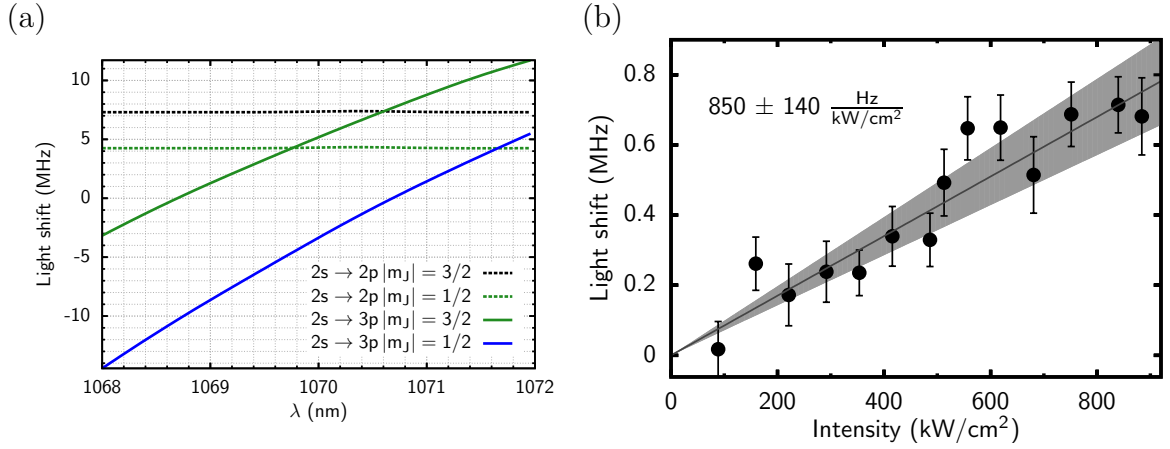


Figure 11.3: (a) Differential AC Stark shift of the  $2S_{1/2} \rightarrow 2P_{3/2}$  and  $2S_{1/2} \rightarrow 3P_{3/2}$  transitions as a function of wavelength for an intensity of  $910 \text{ kW}/\text{cm}^2$ , calculation by M. Safronova (personal communication). The color code is the same as in Fig. 11.2. (b) Differential AC Stark shift of the  $2S_{1/2} \rightarrow 3P_{3/2}$  transition as a function of intensity of the optical trapping light at  $\lambda = 1070 \text{ nm}$ . The circles represent the center of a Gaussian fit of a loss resonance and the error bars are  $1 \sigma$  statistical error of these fits. The solid line is a linear fit to the resonance position with a slope of  $850(140) \text{ Hz}/(\text{kW}/\text{cm}^2)$ , where the error represents the statistical uncertainty of the fit and a systematic uncertainty of 10% on the value of the trap intensity. The gray shaded region indicates the error of the linear fit.

temperature in the MOT.

## Conclusion

---

In this thesis I have described the first realization of narrow linewidth cooling of  $^6\text{Li}$  atoms. In conjunction with a 1070 nm optical dipole trap, narrow linewidth cooling has proved to be an excellent tool for the creation of a degenerate Fermi gas. The fact that the light shift in the 1070 nm trap is small and to the blue ensures that laser cooling is effective throughout the trap volume, providing an efficient way of loading the atoms from the narrow line MOT into the trap. After evaporation in the optical trap at  $280\ a_0$ , we are able to reach numbers in degenerate samples that only had been attained before with much slower duty-cycle sympathetic cooling experiments.

The fast and efficient production of degenerate Fermi gases provides an excellent starting point for future experiments. We are currently implementing a three dimensional optical lattice to study the rich physics of the Fermi-Hubbard model.  $^6\text{Li}$  atoms in an optical lattice with controllable interactions can be described by the Fermi-Hubbard Hamiltonian for a two-spin component Fermi gas. This Hamiltonian is relevant for understating strongly correlated electron systems and in particular it may capture the essential physics responsible for high- $T_c$  superconductivity [42]

Our next milestone is to search for evidence of the antiferromagnetically ordered Néel state, that is known to occur in the normal phase of the Fermi-Hubbard model at half-filling. We will try to detect the antiferromagnetic state by use of a Bragg scattering technique [43]. The geometry of Apparatus3 was specifically chosen to accommodate the angles necessary for the detection of antiferromagnetism with Bragg

---

scattering. After four long years of building up, Apparatus3 is finally approaching the physics which it was meant to study.

## BIBLIOGRAPHY

---

- [1] B. DeMarco and D. S. Jin, “Onset of Fermi Degeneracy in a Trapped Atomic Gas,” *Science* **285**, 1703–1706 (1999).
- [2] M. H. Anderson, J. R. Ensher, M. R. Matthews, C. E. Wieman, and E. A. Cornell, “Observation of Bose-Einstein Condensation in a Dilute Atomic Vapor,” *Science* **269**, 198–201 (1995).
- [3] C. C. Bradley, C. A. Sackett, J. J. Tollett, and R. G. Hulet, “Evidence of Bose-Einstein Condensation in an Atomic Gas with Attractive Interactions,” *Phys. Rev. Lett.* **75**, 1687–1690 (1995).
- [4] K. B. Davis, M. O. Mewes, M. R. Andrews, N. J. van Druten, D. S. Durfee, D. M. Kurn, and W. Ketterle, “Bose-Einstein Condensation in a Gas of Sodium Atoms,” *Phys. Rev. Lett.* **75**, 3969–3973 (1995).
- [5] Z.-C. Yan, J. F. Babb, A. Dalgarno, and G. W. F. Drake, “Variational calculations of dispersion coefficients for interactions among H, He, and Li atoms,” *Phys. Rev. A* **54**, 2824–2833 (1996).
- [6] A. G. Truscott, K. E. Strecker, W. I. McAlexander, G. B. Partridge, and R. G. Hulet, “Observation of Fermi Pressure in a Gas of Trapped Atoms,” *Science* **291**, 2570–2572 (2001).
- [7] F. Schreck, L. Khaykovich, K. L. Corwin, G. Ferrari, T. Bourdel, J. Cubizolles,

- and C. Salomon, “Quasipure Bose-Einstein Condensate Immersed in a Fermi Sea,” *Phys. Rev. Lett.* **87**, 080403 (2001).
- [8] Z. Hadzibabic, C. A. Stan, K. Dieckmann, S. Gupta, M. W. Zwierlein, A. Görlitz, and W. Ketterle, “Two-Species Mixture of Quantum Degenerate Bose and Fermi Gases,” *Phys. Rev. Lett.* **88**, 160401 (2002).
- [9] C. Silber, S. Günther, C. Marzok, B. Deh, P. W. Courteille, and C. Zimmermann, “Quantum-Degenerate Mixture of Fermionic Lithium and Bosonic Rubidium Gases,” *Phys. Rev. Lett.* **95**, 170408 (2005).
- [10] M. D. Barrett, J. A. Sauer, and M. S. Chapman, “All-Optical Formation of an Atomic Bose-Einstein Condensate,” *Phys. Rev. Lett.* **87**, 010404 (2001).
- [11] S. R. Granade, M. E. Gehm, K. M. O’Hara, and J. E. Thomas, “All-Optical Production of a Degenerate Fermi Gas,” *Phys. Rev. Lett.* **88**, 120405 (2002).
- [12] K. M. O’Hara, S. L. Hemmer, M. E. Gehm, S. R. Granade, and J. E. Thomas, “Observation of a Strongly Interacting Degenerate Fermi Gas of Atoms,” *Science* **298**, 2179–2182 (2002).
- [13] T. Weber, J. Herbig, M. Mark, H.-C. Nägerl, and R. Grimm, “Bose-Einstein Condensation of Cesium,” *Science* **299**, 232–235 (2003).
- [14] S. Jochim, M. Bartenstein, A. Altmeyer, G. Hendl, S. Riedl, C. Chin, J. Hecker Denschlag, and R. Grimm, “Bose-Einstein Condensation of Molecules,” *Science* **302**, 2101–2103 (2003).
- [15] C.-L. Hung, X. Zhang, N. Gemelke, and C. Chin, “Accelerating evaporative cooling of atoms into Bose-Einstein condensation in optical traps,” *Phys. Rev. A* **78**, 011604 (2008).



- 
- [16] J.-F. Clément, J.-P. Brantut, M. Robert-de Saint-Vincent, R. A. Nyman, A. Aspect, T. Bourdel, and P. Bouyer, “All-optical runaway evaporation to Bose-Einstein condensation,” *Phys. Rev. A* **79**, 061406 (2009).
- [17] X. Du, Y. Zhang, and J. E. Thomas, “Inelastic Collisions of a Fermi Gas in the BEC-BCS Crossover,” *Phys. Rev. Lett.* **102**, 250402 (2009).
- [18] T. Hänsch and A. Schawlow, “Cooling of gases by laser radiation,” *Opt. Commun.* **13**, 68 – 69 (1975).
- [19] D. Wineland and H. Dehmelt, *Bull. Am. Phys. Soc.* **20**, 637 (1975).
- [20] J. Dalibard and C. Cohen-Tannoudji, “Laser cooling below the Doppler limit by polarization gradients: simple theoretical models,” *J. Opt. Soc. Am. B* **6**, 2023–2045 (1989).
- [21] P. J. Ungar, D. S. Weiss, E. Riis, and S. Chu, “Optical molasses and multilevel atoms: theory,” *J. Opt. Soc. Am. B* **6**, 2058–2071 (1989).
- [22] D. S. Weiss, E. Riis, Y. Shevy, P. J. Ungar, and S. Chu, “Optical molasses and multilevel atoms: experiment,” *J. Opt. Soc. Am. B* **6**, 2072–2083 (1989).
- [23] P. D. Lett, W. D. Phillips, S. L. Rolston, C. E. Tanner, R. N. Watts, and C. I. Westbrook, “Optical molasses,” *J. Opt. Soc. Am. B* **6**, 2084–2107 (1989).
- [24] G. Ritt, G. Cennini, C. Geckeler, and M. Weitz, “Laser frequency offset locking using a side of filter technique,” *Applied Physics B: Lasers and Optics* **79**, 363–365 (2004), 10.1007/s00340-004-1559-6.
- [25] G. Ferrari, M.-O. Mewes, F. Schreck, and C. Salomon, “High-power multiple-frequency narrow-linewidth laser source based on a semiconductor tapered amplifier,” *Opt. Lett.* **24**, 151–153 (1999).

- 
- [26] K. Sowka, M. Weel, S. Cauchi, L. Cockins, and A. Kumarakrishnan, “A home-built lock-in amplifier for laser frequency stabilization,” *Canadian Journal of Physics* **83**, 907–918 (2005).
- [27] C. R. Vidal and J. Cooper, “Heat Pipe Oven: A New, Well Defined Metal Vapor Device for Spectroscopic Measurements,” *J. Appl. Phys* **40**, 3370–3374 (1969).
- [28] C. R. Vidal and F. B. Haller, “Heat Pipe Oven Applications. I. Isothermal Heater of Well Defined Temperature. II. Production of Metal Vapor-Gas Mixtures,” *Rev. Sci. Instrum.* **42**, 1779–1784 (1971).
- [29] I. E. Olivares, A. E. Duarte, T. Lokajczyk, A. Dinklage, and F. J. Duarte, “Doppler-free spectroscopy and collisional studies with tunable diode lasers of lithium isotopes in a heat-pipe oven,” *J. Opt. Soc. Am. B* **15**, 1932–1939 (1998).
- [30] M. Junker, Ph.D. thesis, Rice University, 2007.
- [31] W. I. McAlexander, E. R. I. Abraham, and R. G. Hulet, “Radiative lifetime of the  $2P$  state of lithium,” *Phys. Rev. A* **54**, R5–R8 (1996).
- [32] R. Kamar, Master’s thesis, Rice University, 2006.
- [33] R. E. Scholten, “Enhanced laser shutter using a hard disk drive rotary voice-coil actuator,” *Rev. Sci. Instrum.* **78**, 026101 (2007).
- [34] A. Nadeem and S. U. Haq, “Photoionization from the  $5p^2P_{3/2}$  state of rubidium,” *Phys. Rev. A* **83**, 063404 (2011).
- [35] M. E. Gehm, S. L. Hemmer, K. M. O’Hara, and J. E. Thomas, “Unitarity-limited elastic collision rate in a harmonically trapped Fermi gas,” *Phys. Rev. A* **68**, 011603 (2003).

- 
- [36] D. A. Butts and D. S. Rokhsar, “Trapped Fermi gases,” *Phys. Rev. A* **55**, 4346–4350 (1997).
- [37] B. DeMarco, Ph.D. thesis, University of Colorado, 2001.
- [38] W. Ketterle and M. W. Zwierlein, “Making, probing and understanding ultracold Fermi Gases,” *Rivista del Nuovo Cimento* **31**, 247–422 (2008).
- [39] H. Katori, M. Takamoto, V. G. Pal’chikov, and V. D. Ovsiannikov, “Ultrastable Optical Clock with Neutral Atoms in an Engineered Light Shift Trap,” *Phys. Rev. Lett.* **91**, 173005 (2003).
- [40] M. S. Safronova, B. Arora, and C. W. Clark, “Frequency-dependent polarizabilities of alkali-metal atoms from ultraviolet through infrared spectral regions,” *Phys. Rev. A* **73**, 022505 (2006).
- [41] J. Mitroy, M. S. Safronova, and C. W. Clark, “Theory and applications of atomic and ionic polarizabilities,” *Journal of Physics B: Atomic, Molecular and Optical Physics* **43**, 202001 (2010).
- [42] P. W. Anderson, “Superconductivity in High  $T_c$  Cuprates: The Cause is No Longer A Mystery,” *Physica Scripta* **2002**, 10 (2002).
- [43] T. A. Corcovilos, S. K. Baur, J. M. Hitchcock, E. J. Mueller, and R. G. Hulet, “Detecting antiferromagnetism of atoms in an optical lattice via optical Bragg scattering,” *Phys. Rev. A* **81**, 013415 (2010).